AGU ADVANCING EARTH AND SPACE SCIENCE

Water Resources Research

RESEARCH ARTICLE
10.1029/2022WR032683

Windmapper: An Efficient Wind Downscaling Method for Hydrological Models

Christopher B. Marsh[1], **Vincent Vionnet**[2], **and John W. Pomeroy**[1]

[1]Centre for Hydrology, University of Saskatchewan, Saskatoon, SK, Canada, [2]Meteorological Research Division, Environment and Climate Change, Gatineau, QC, Canada

Key Points:

- New software for wind library generation
- Lower error in speed and direction that other empirical models
- Applicable to large extents over 1M km^2

Correspondence to:

C. B. Marsh,
chris.marsh@usask.ca

Citation:

Marsh, C. B., Vionnet, V., & Pomeroy, J. W. (2023). Windmapper: An efficient wind downscaling method for hydrological models. *Water Resources Research*, *59*, e2022WR032683. https://doi.org/10.1029/2022WR032683

Received 26 APR 2022
Accepted 1 MAR 2023

Author Contributions:

Conceptualization: Christopher B. Marsh, Vincent Vionnet, John W. Pomeroy
Data curation: John W. Pomeroy
Funding acquisition: John W. Pomeroy
Methodology: Christopher B. Marsh, Vincent Vionnet, John W. Pomeroy
Software: Christopher B. Marsh, Vincent Vionnet
Validation: Christopher B. Marsh, Vincent Vionnet
Visualization: Christopher B. Marsh
Writing – original draft: Christopher B. Marsh, Vincent Vionnet, John W. Pomeroy
Writing – review & editing: Christopher B. Marsh, Vincent Vionnet, John W. Pomeroy

Abstract Estimates of near-surface wind speed and direction are key meteorological components for predicting many surface hydrometeorological processes that influence critical aspects of hydrological and biological systems. However, observations of near-surface wind are typically spatially sparse. The use of these sparse wind fields to force distributed models, such as hydrological models, is greatly complicated in complex terrain, such as mountain headwaters basins. In these regions, wind flows are heavily impacted by overlapping influences of terrain at different scales. This can have a great impact on calculations of evapotranspiration, snowmelt, and blowing snow transport and sublimation. The use of high-resolution atmospheric models allows for numerical weather prediction (NWP) model outputs to be dynamically downscaled. However, the computation burden for large spatial extents and long periods of time often precludes their use. Here, a wind-library approach is presented to aid in downscaling NWP outputs and terrain-correcting spatially interpolated observations. This approach preserves important spatial characteristics of the flow field at a fraction of the computational costs of even the simplest high-resolution atmospheric models. This approach improves on previous implementations by: scaling to large spatial extents O(1M km^2); approximating lee-side effects; and fully automating the creation of the wind library. Overall, this approach was shown to have a third quartile RMSE of 1.8 m · s^{-1} and a third quartile RMSE of 58.2° versus a standalone diagnostic windflow model. The wind velocity estimates versus observations were better than existing empirical terrain-based estimates and computational savings were approximately 100-fold versus the diagnostic model.

1. Introduction

Estimates of near-surface wind speed and direction are key meteorological components for predicting many surface processes that influence critical aspects of the hydrological and biological systems. Examples include: horizontal snow mass redistribution (Marsh et al., 2019; Mott et al., 2010; Pomeroy et al., 1997; Pomeroy & Li, 2000; Winstral et al., 2013), forest fire path prediction (Forthofer et al., 2014; Quill et al., 2019), blowing snow sublimation (Pomeroy & Essery, 1999; Pomeroy & Male, 1992), rain-on-snow events (Vionnet et al., 2020), ecological system conservation and management (Liston et al., 2016), snow-vegetation interactions (Lumbrazo et al., 2022; Lundquist et al., 2021; Sturm et al., 2001), lake turbulent fluxes (Sugita et al., 2020), evapotranspiration (Ravazzani et al., 2020; Schymanski & Or, 2016), and insect and pathogen transport (Luo et al., 2008). Near-surface wind velocities tend to be quite variable over short spatial and temporal scales, motivating a dense observation network (Luo et al., 2008). However, near-surface wind velocity (herein, velocity is describing a vector that represents the speed and direction) observations are typically spatially sparse outside of research domains (Mott et al., 2018). Thus, despite the importance of these wind observations, the spatially sparse observation networks can be problematic for application in spatially distributed applications, such as numerical models.

In complex terrain, wind flows are heavily impacted by overlapping influences of terrain at different scales (Ryan, 1977; Wood, 2000). Spatially and temporally variable wind velocities arise due to complex topographic and vegetation interactions with meso- and micro-scale topography where wind accelerates over hills and ridge crests (Jackson & Hunt, 1975; Mason & Sykes, 1979; Walmsley et al., 1984; Wood, 2000) and decelerates over lee slopes, in topographic depressions, and behind tall vegetation (Tabler et al., 1990). Thermally driven wind systems can also develop at different scales (individual slope, valley, whole mountain range) due to diurnal variation in the surface energy budget in complex topography (Reynolds et al., 2021; Serafin et al., 2018; Stewart et al., 2002). Individual point observations cannot be simply spatially interpolated due to the profound impacts of topography (Ryan, 1977).

The problem of limited data is further compounded in remote locales, such as the critically important mountain headwaters that act as the water towers of the world (Viviroli et al., 2007). In these mountain headwaters, winter winds heavily influence the heterogeneity of snowpacks (Fang & Pomeroy, 2009; Freudiger et al., 2017; MacDonald et al., 2009, 2010; Marsh & Pomeroy, 1999; Mott et al., 2010, 2018; Pomeroy, 1991; Pomeroy et al., 1997; Sturm et al., 2001; Wayand et al., 2018; Winstral et al., 2013) that can have profound impacts on downstream water resources (Dornes, Pomeroy, Pietroniro, & Verseghy, 2008; Fang et al., 2013; Luce et al., 1998; Marsh & Pomeroy, 1996; Pomeroy et al., 1997; Vionnet et al., 2020; Woo & Thorne, 2006). The use of spatially distributed hydrological models in these areas for prediction of water resources is motivated by the desire to explicitly represent these small-scale system behaviors and state variables (Dornes, Pomeroy, Pietroniro, Carey, & Quinton, 2008; Fatichi et al., 2016; Marsh et al., 2020). This is often done by representing the topography at snow-drift permitting length scales of sub-200 m (Pomeroy et al., 2015; Vionnet et al., 2021). Due to the sparse observation network of near-surface winds, predictions in these often ungauged regions increasingly relies on downscaling coarse-scale numerical weather prediction (NWP) system output to estimate local wind velocities (Barcons et al., 2018; Vionnet et al., 2017; Wagenbrenner et al., 2016). Downscaling is required as the length scale of these NWP outputs is typically on the order of several kilometers. At these scales, the complex topography is too homogenous and results in insufficiently representing the impacts of complex terrain (Barcons et al., 2018; Vionnet et al., 2021). There is therefore a significant desire to account for the small-scale, spatially variable wind fields due to terrain influences.

The modeling approaches to estimate the spatially distributed topographic impacts on wind velocities at sub-200 m scales are applicable to both terrain-correcting interpolated values (e.g., spatial interpolation between observed values at meteorological stations) and to downscaling of NWP output. Computationally complex methods for dynamically downscaling wind fields, such as computational fluid dynamics (CFD) and Large Eddy Simulation (LES) models can provide detailed estimates of near-surface wind velocity (Vionnet et al., 2017; Wagenbrenner et al., 2019; Wang & Huang, 2017). However, they require substantial computational resources and can be numerically unstable in highly complex terrain. Diagnostic models that preserve mass-conservation but neglect momentum conservation can allow for decreased sensitivity to surface roughness and boundary layer conditions as well as result in faster numerical solutions (Quill et al., 2019). However, neglecting momentum conservation produces limitations in leeward slopes where recirculation and flow separation are not accounted for (Quill et al., 2019; Wagenbrenner et al., 2016). Simpler parameterizations derived from parametric fits to wind tunnel data and CFD models, such as those of Walmsley et al. (1984) and Walmsley et al. (1989) provide computationally efficient estimates of crest windspeeds. However, these parameterizations were developed for isolated hills and are difficult to apply to spatially distributed applications. Linearized approaches, such as MS3DJH/3R (Walmsley et al., 1986) are applicable for low hills (Walmsley et al., 1986) with slopes of no more than 1 in 4 (Essery et al., 1999). These limitations make application to mountain regions difficult. Topographic feature methods, such as the popular MicroMet code of Liston and Elder (2006), estimate the impact of terrain on the speed via terrain curvatures. The impact of terrain on wind direction is then estimated using parameterizations such as that of Ryan (1977). The MicroMet approach has received substantial usage in spatially distributed hydrological models, especially when applied to complex terrain, for example, Pohl et al. (2006), Liston et al. (2007), Bernhardt et al. (2012), Musselman et al. (2015), Ravazzani et al. (2020), and Mills et al. (2019). However, its empirical nature requires calibration (Pohl et al., 2006), and the directional perturbations are limited to a maximum diversion of 22.5° (Ryan, 1977) which can be problematic for simulating some processes such as blowing snow (Mills et al., 2019; Musselman et al., 2015). Terrain sheltering indexes such as Winstral et al. (2009) have shown some success (Winstral et al., 2017), however only provide speed, not direction estimates. Lastly, another approach has been to pre-compute terrain impacts on windflow via a more complex atmospheric models and "look-up" the perturbations at run time. To reduce the computational cost of using a high-resolution wind model, Lehning et al. (2008) decomposed a simulation period into periods of quasi-stationary conditions. Then, time-averaged observations for these periods were used as boundary conditions to produce a library of wind fields for four wind speed conditions and eight wind directions. Bernhardt et al. (2009) used a 220 wind field library that represented the most relevant synoptic situations for wind-induced snow transport at their test site. Instead of using the wind speeds directly, Essery et al. (1999) and Barcons et al. (2018) used an approach of normalizing the terrain impacts into speedup-factors, which then perturbed spatially interpolated observations.

In summary, distributed land surface scheme models motivate the inclusion of distributed wind fields. Unfortunately, the computational overhead and increased data requirements of high-resolution atmospheric models prohibits extensive use for either long periods of simulation, large spatial extents, or fine-scale spatial resolutions. The isolated hill parameterizations, for example, Walmsley et al. (1989), are difficult to map to the spatial variable topographic of complex terrain, but have been included in some models such as the Cold Regions Hydrological Model (CRHM) (Pomeroy et al., 2007, 2022). Curvature methods tend to require calibration against observations, have limited wind direction modification in complex terrain, and are limited in the total domain size due to how the maximum curvature is normalized. These limitations are further complicated as wind flow models that perform well at a point may not provide satisfactory spatial heterogeneity, thus limiting application for other processes such as blowing snow (Musselman et al., 2015). Therefore, there is a need for a method that is computationally efficient, applicable for large spatial extents, provides substantial direction changes in complex terrain, and can be used for key processes such as blowing snow.

A new software tool Windmapper is presented that allows for efficient downscaling and interpolation of wind fields. Windmapper extends the wind library approaches of Essery et al. (1999) and Barcons et al. (2018) by using the diagnostic, mass conserving windflow model WindNinja (Wagenbrenner et al., 2016). Unique to this approach is that wind direction perturbations are also calculated using the table lookup approach, which allows for greater divergence in wind field direction fields. It also enables lee-side effects. It is designed for easy inclusion into land surface and hydrological models where small-scale wind fields are of critical importance. Specifically, the following questions arise: (a) how much error is introduced by this simplification versus the fully "online" windflow model used to generate the library; (b) can this approach be used with an unstructured surface representation; and; (c) what uncertainties are associated with the use of a fixed number of wind directions?

2. Model Development

2.1. Overview

WindMapper is a tool to help downscale mesoscale windfields, such as those from numerical weather prediction systems at 2.5 km resolution, to microscale winds used in fine-grained land surface models at, e.g., a 50 m resolution. This approach is an extension of the approaches developed by Essery et al. (1999) and Barcons et al. (2018) and applied to unstructured meshes by Marsh et al. (2019) and Vionnet et al. (2021). In brief: a mass-conserving diagnostic windflow model is used to determine the mechanical terrain impacts on a windflow field for a set of fixed wind directions, for example, from the North, East, South, West. Once normalized, these flow fields are saved into a library of speedup and direction perturbation maps allowing for fast lookup of relative windspeeds across the simulation domain at runtime for the consuming model.

The Windmapper tool is two discrete components: (a) a Python code that automates the creation of the wind field library (a set of wind field maps) and (b) the use of the wind library in a model to downscale winds. The Windmapper code and algorithm were designed for use in a spatially distributed model or for use in parameterizing semi-distributed models such as those based on the hydrological response unit (HRU) approach (Flügel, 1995). The use of the wind library in a spatially distributed model is model agnostic. Herein, examples are shown as used by the Canadian Hydrological Model (CHM) (Marsh et al., 2020). A full implementation of the Windmapper algorithms are available in CHM, however basic usage examples are provided in the Windmapper repository (please see Code Availability section for details). Although Windmapper is currently dependent upon the WindNinja model for producing the wind library, there is no limitation that precludes another windflow model from being used. WindNinja was selected due to: being open source; available in a fast-running mass conserving diagnostic configuration; actively developed; and provided reasonable estimates of wind velocity when tested. A preliminary version of Windmapper was partly described by Vionnet et al. (2021) and was used by Marsh et al. (2019) and Vionnet et al. (2021) when simulating snowpack evolution in the Canadian sub-Arctic and Canadian Rockies respectively.

The processing workflow is described below at a high-level, with the following sections providing more background on the algorithm. The high-level workflow is as follows and illustrated in Figure 1:

1. Select domain
2. Determine number of directions to be in the wind library
3. Determine spatial resolution of the windflow model
4. Run underlying wind model for those directions
5. Use the output in a land-surface model

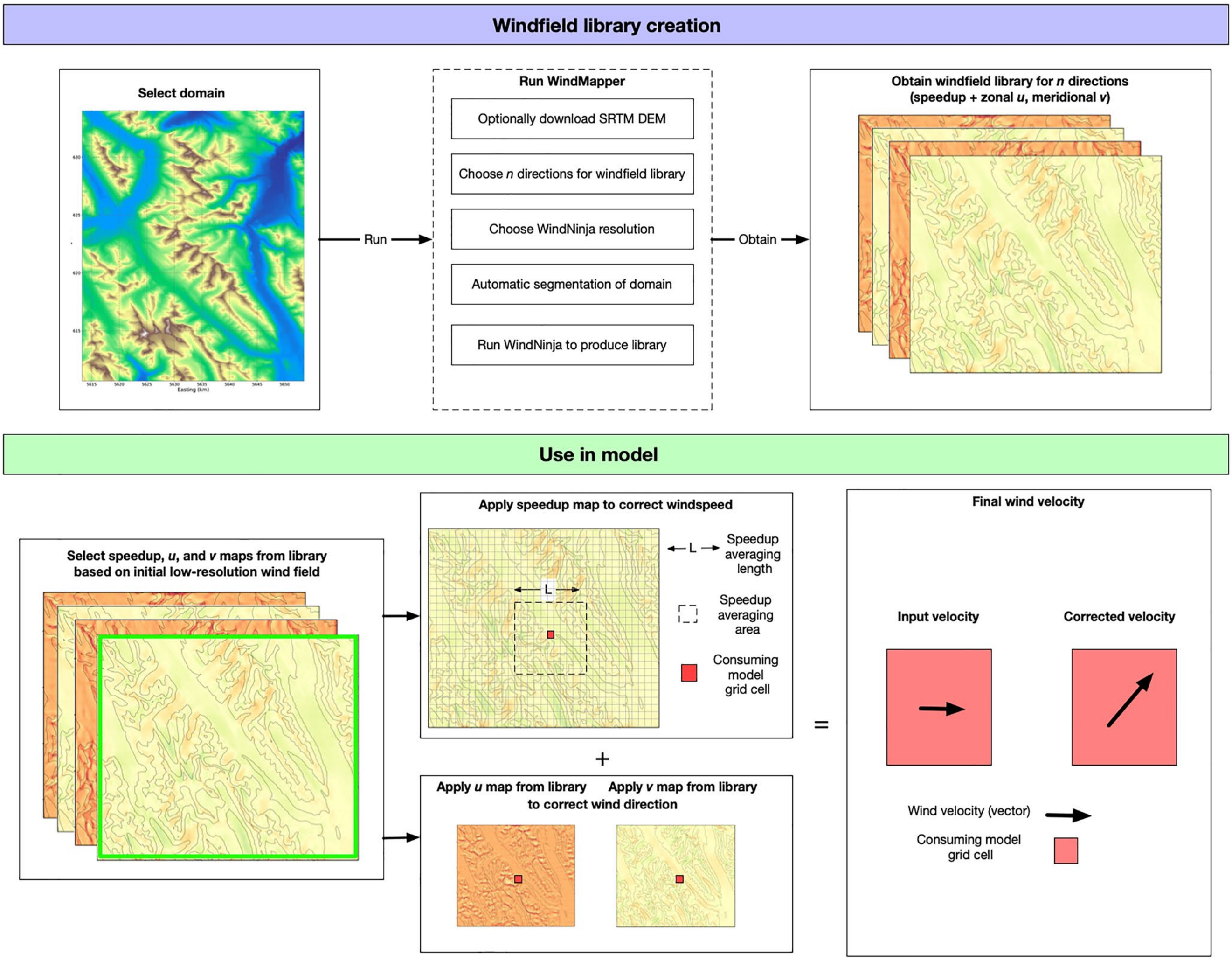

Figure 1. A simplified overview of the WindMapper workflow. The domain is selected and various parameters are customized by the user before WindMapper runs the WindNinja wind model to produce the wind field library. When this wind field library is to be used in a model, the initial, to-be-corrected, coarse windfield is used to select the speedup and direction perturbation maps. These are used to modify the wind velocity at each computational element (e.g., grid cell; red square in diagram). The input elevation *x*/*y* axes are UTM 11N metres.

For an end-user perspective, the two primary decisions required are: (a) what spatial resolution to run the wind-flow pre-processing steps at and (b) how many wind directions should be produced for the library. The spatial resolution should be sufficient to capture the micro-scale topography that is known to impact the wind flow, as well as being approximately the same order of magnitude as the spatial discretization used in the ingesting model. The number of wind directions ensures that more variability in the spatial fields is possible but at a minimum 12 and no more than 24 has been deemed sufficient by the authors (Marsh et al., 2019; Vionnet et al., 2021). These decisions are investigated in the uncertainty analysis section.

Both CHM and Windmapper are open source software. Windmapper is installable via Python *pip*. This automates the compilation of the WindNinja backend and ensures ease of use from within a Python virtual environment. Further details can be found in the respective documentation, detailed in the Data Availability Section.

2.2. Wind Field Library

The impact of terrain on micro-scale wind fields are precomputed using the diagnostic mass-conserving wind-flow model WindNinja (Wagenbrenner et al., 2016). WindNinja was primarily designed to capture the mechanical effects of terrain on wind flow and has been shown to generally capture the important features of terrain-induced wind flow in complex terrain, such as ridge-top acceleration and valley channeling (Forthofer et al., 2014).

10.1029/2022WR032683

To compute the wind field library, WindNinja is run with a constant input wind speed from N cardinal directions at some fixed spatial resolution. The finer this resolution, the more micro-topography is incorporated into the wind library. The optional configuration to include thermally driven windflow is not used. Thus, a user-specified spatial extent may be provided. This extent is used to automatically download the digital elevation model (DEM) required to run the simulations. Currently, this is the Shuttle Radar Topographic Model (SRTM) 30 m DEM (Farr et al., 2007) however this approach also works with user-supplied DEMs. A spatially constant initial condition of wind speed ($10\,\mathrm{m}\cdot\mathrm{s}^{-1}$) and a bare-earth roughness length ($z_0 = 0.01°$ m) are used to initialize WindNinja. If vegetation interactions or other surface characteristic impacts are desired, these can be included later in the consumer model as appropriate, however they are not considered at this step. For each wind direction, the transfer function f is computed as:

$$f = \frac{U_{WN}}{< U_{WN} >_L} \tag{1}$$

where U_{WN} is the local wind speed (i.e., $U_{WN} = \sqrt{u_{WN}^2 + v_{WN}^2}$), u_{WN} and v_{WN} are the horizontal components of the wind vector, and $< U_{WN} >_L$ is the spatial average of U_{WN} over an area of the size $L \times L$. L is user configurable.

By construction, as $L \rightarrow 0$ then $f \rightarrow 1$. As L decreases, f incorporates fewer of the local wind fluctuation induced by the micro-scale terrain features (Barcons et al., 2018). Note that Barcons et al. (2018) used a circle instead of a square to compute the spatial average of the wind speed. Thus, f acts as a speedup/slowdown factor that accounts for topographic impacts on wind speed. The resulting output of the wind library is a set of raster files with u_{WN}, v_{WN}, and transfer function components as computed by Equation 1.

If the simulation extent is greater than the L area given above, then the domain is automatically tiled into the correct number of subdomains by Windmapper. Each of the subdomains are slightly larger than optimal to ensure a good overlap in the wind solution between different subdomains. These subdomains are run in parallel to generate the wind library, dramatically decreasing the computational time required for large domains. The overlapping regions are combined by taking the mean of all overlapping regions.

An example of wind field library for some arbitrary mountain topography is shown in Figure 2 where the top row shows a constant wind from the North (N) for the magnitude (top-left), zonal u (N.u; top-middle), and meridional v (N.v; top-right). This is repeated in the bottom row for a wind from the West (W).

2.3. Adjustment of Wind Speed and Direction

Once the wind field library is created, the following algorithm is used to correct a spatially complete initial condition wind field for mechanical topographic impacts. This input wind field may be because of spatially interpolating observed wind velocities, or it could be interpolated NWP output. In any case, each computational element (i.e., raster cell, triangle) should have a wind speed (w; $\mathrm{m}\cdot\mathrm{s}^{-1}$), zonal u (toward East; $\mathrm{m}\cdot\mathrm{s}^{-1}$), and meridional v (toward north; $\mathrm{m}\cdot\mathrm{s}^{-1}$) component. Typically, windspeed and wind direction (θ) are given and these can be converted to u, v components as follows (Liston & Elder, 2006):

$$u = -w \cdot \sin(\theta), \tag{2}$$

$$v = -w \cdot \cos(\theta) \tag{3}$$

where the sign convention is a meteorological wind direction such that the wind flows *from* this direction and direction is clockwise from North.

The example of the algorithm, described below, is a simple, idealized case and as such assumes there are four lookup maps: East (90°), South (180°), West (270°), and North (0°). Thus, each library item covers ($\Delta\theta = 90^{\circ}$). The wind library is constructed such that the library items have indexes 1, 2, 3, 4 respectively with the first index (i.e., 1) corresponding to direction $0 + \Delta\theta$. This approach can easily be changed to incorporate 0-indexing if preferred.

Step 1. Interpolation

10.1029/2022WR032683

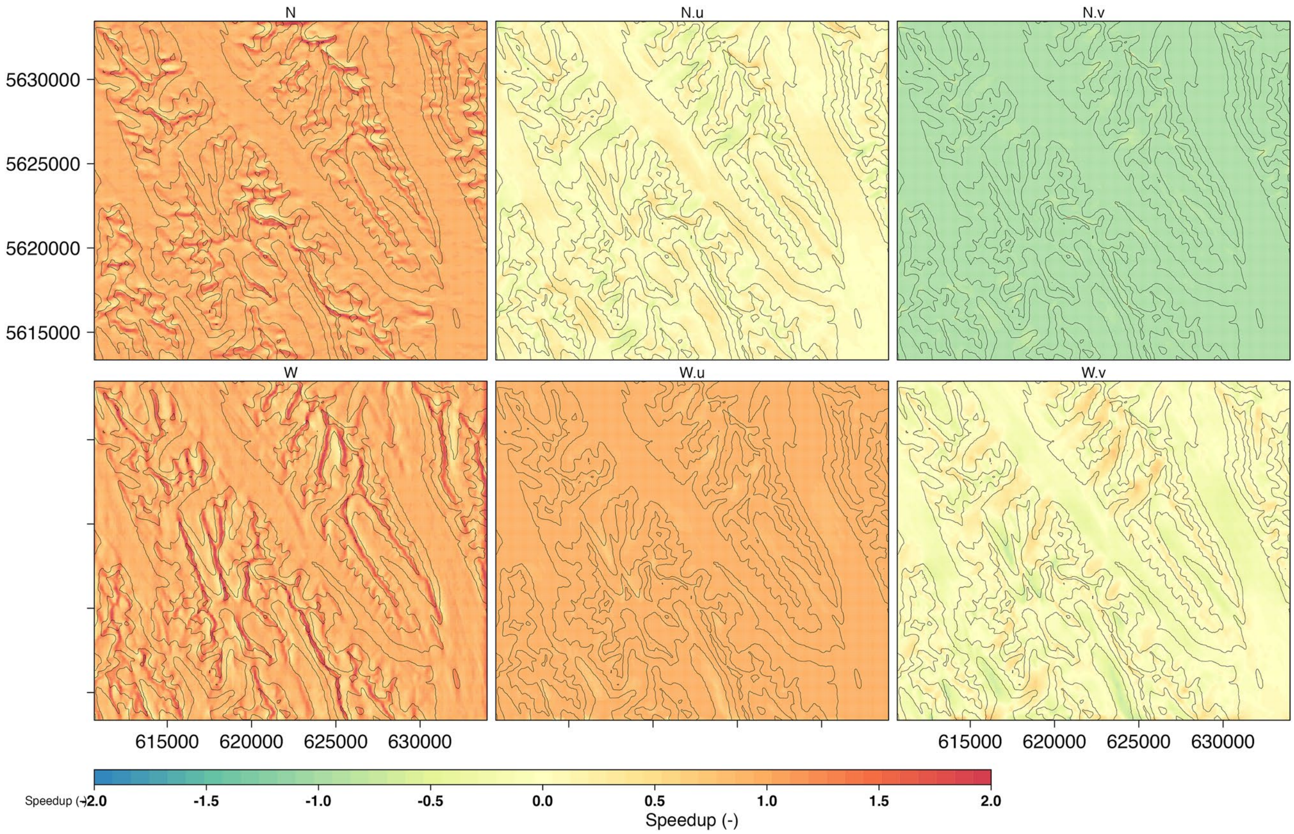

Figure 2. An example of a North (N) and West (W) wind library map (50 m spatial resolution) showing the speedup (−), zonal u (X.u), and meridional v (X.v) components at 40 m reference height. The u and v maps ignore magnitude and are only used to reconstruct the direction perturbation. Elevation contours are every 300 m and *x*/*y* axes are UTM 11N metres.

Interpolate input windspeed and direction to the model domain using a method such as thin plate splines with tension (e.g., Chang (2008)) or inverse distance weighting (e.g., Chang (2008)). When interpolating the wind direction ensure the u and v components are interpolated instead of θ to avoid problems crossing the $360^{\circ}/0^{\circ}$ direction line (Liston & Elder, 2006). The zonal and meridional components can be recombined to a direction:

$$\Theta = a\tan 2(-u, -v). \tag{4}$$

Note that different implementations of arctan2 exist and may report a negative value for due north, for example,

$$a\tan 2(0, 1) = -\pi. \tag{5}$$

This can be corrected by adding 2π for $\theta < 0$.

For the following example, a uniform spatial interpolation was used for simplicity. These initial conditions are:

1. Constant wind velocity across the domain
2. Wind from direction = 270°
3. Wind speed at 40 m = 10 $\mathrm{m} \cdot \mathrm{s}^{-1}$

This initial condition is shown in the top-left in Figure 3 where the arrows denote the wind direction, and the coloured cell values denote the windspeed ($\mathrm{m} \cdot \mathrm{s}^{-1}$). The initial condition windspeed was (arbitrarily) selected to approximately correspond to the mean wind speed during events driven by large scale meteorology in the study area. However, any "reasonable" constant input is considered to be correct due to the normalization that occurs.

Step 2. Wind library lookup

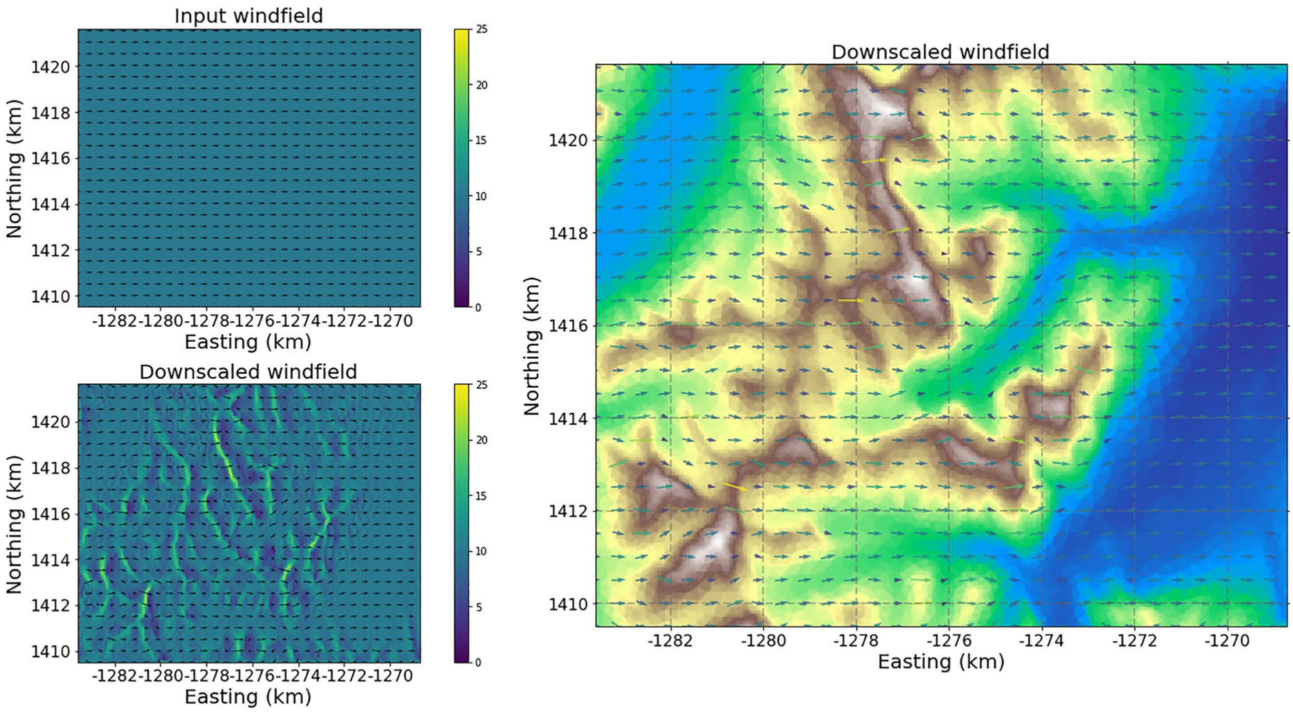

Figure 3. An example of the algorithm applied to an uniform input wind velocity of 10 m · s^{-1} from the direction $\theta = 270^{\circ}$. Arrows denote wind direction (toward arrow head) and colour indicates speed (m · s^{-1}). This shows the three steps of the algorithm from initial wind field (top left) and the perturbation of direction and speed (bottom left). The right-hand side shows a zoomed in view of this domain to better illustrate the perturbations in direction possible with this algorithm. The x and y axes are UTM 11N metres.

For each computational cell in the ingesting model (herein, computational cell will be referred to as "cell"), look up which library map d to use based on wind direction θ:

$$d = \lfloor \theta / \Delta\theta \rfloor \tag{6}$$

where θ is the interpolated direction found above, and $\Delta\theta$ ($^{\circ}$) is the angle each wind map covers. The d value is an index into the windmap library. If $d = 0$ then set $d = \theta_n$ where θ_n is the total number of wind field maps. Note that each cell will likely have a different d value. For this example,

$$d = \lfloor 270^{\circ} / 90^{\circ} \rfloor = 3. \tag{7}$$

As there is a uniform direction as the given initial conditions, each cell will use lookup map $d = 3$.

Step 3. Direction

The new wind direction only for the cell can be derived directly from the u and v lookup maps. Thus, choose the u and v map that corresponds to index d and perturb the cell's u and v component to that of direction map d's u and v component. The direction can be recovered from the u and v components via Equation 4. The output u and v maps are only use to reconstruct direction due to including a uniformly constant windspeed of 1 m · s^{-1}; that is, $w = 1$ in Equation 3.

This step is shown in Figure 3, bottom left where the new direction is shown. The underlying colours are from the next step.

Step 4. Speed

To perturb the wind speed, the previously computed d value is used to look up the transfer function ($f^{i,j}$) for each cell i, j in the 2D domain. Then the corrected windspeed ($W'_{i,j}$) at each cell is

$$W'_{i,j} = W_{i,j} \cdot f^{i,j}. \tag{8}$$

This new wind speed is shown as the colour in Figure 3, bottom left. Shown in Figure 3 right is the same corrected wind field, overlain on the topography for a zoomed-in region. Arrow size and colour correspond to wind speed. This better illustrates the substantial direction divergence that can occur with this method.

Step 5. Optionally, lee-side slowdown

Forthofer et al. (2014) and Wagenbrenner et al. (2016, 2019) have shown that the mass-conserving version of WindNinja has difficulties simulating lee-side recirculation where flow separation occurs. This difficulty is due to the absence of a momentum equation in the mass-conserving version of the WindNinja flow simulation (Forthofer et al., 2014). An optional step in Windmapper may be performed to account for lee-side wind speed reduction. This is done by computing the Winstral et al. (2002) Sx terrain parameter to identify locations in the lee that may be susceptible to flow separation. Computational elements that had a critical angle of Sx > 20° computed from a 300 m range were considered susceptible to flow separation (Vionnet et al., 2021; Wood, 1995). To account for this, the transfer function f was set to 0.25 following Winstral et al. (2009).

A value of 300 m is used in WindMapper as the maximal search distance, d max, when computing Sx. This value was selected since it corresponds to the optimal value reported by Winstral et al. (2009) when developing a method for distributing wind speed in several mountains catchments and by Winstral et al. (2017) when down-scaling wind speed from a numerical weather prediction system in the Swiss Alps.

3. Data and Methods

3.1. Overview

To evaluate the capabilities of Windmapper, two evaluation approaches are used. These are described broadly here and in detail in the following sections.

First, the above detailed algorithm is evaluated by down-scaling NWP output and comparing at a point-scale against observations from several Canadian Rockies Hydrological Observatory research stations in the Canadian Rocky Mountains west of Calgary, Alberta. Although such an evaluation is deeply contingent upon the NWP model producing the correct meso-scale wind patterns, such an evaluation provides insight into: (a) if the algorithm is more accurate than using a coarse NWP; and (b) if the algorithm is on-par or better than other down-scaling algorithms. Inputs for Windmapper are taken here from a NWP system as the observation points are too spatially sparse to spatially interpolate in a meaningful way.

Second, as the WindMapper algorithm is a type of model simplification of the WindNinja model, the Windmapper output is compared directly to the standalone WindNinja output. Specifically, both approaches are used to downscale the same NWP input as above. This evaluation is done spatially so-as to quantifying the spatial pattern of errors introduced by the model simplification. In this study, bare-earth simulations are performed and vegetation is not considered as the goal herein is to compare the bare-earth representations and quantify the error introduced by the model approximation.

3.2. Study Area

The study area is a 958 km^2 domain in the Kananaskis Valley of the Canadian Rockies, Alberta, shown in Figure 4. Characterized by complex topography, elevations range from 1,400 to 3,406 m. This area hosts the University of Saskatchewan's Canadian Rockies Hydrological Observatory (CRHO; https://research-groups.usask.ca/hydrology/science/research-facilities/crho.php) surface meteorological network, detailed in the next section. The climate is dominated by continental air masses with long and cold winters. In the northern portion of this study region, these cold winters are interrupted by frequent mid-winter chinooks (Foehns) (DeBeer & Pomeroy, 2009). Snow covers the upper elevations from October to June (DeBeer & Pomeroy, 2009; Harder et al., 2016).

3.3. Meteorological Observations

Observed windspeed and direction were obtained at an hourly interval from the CRHO data set including stations from the Marmot Creek Research Basin (Fang et al., 2019) and the Fortress Mountain Research Basin (Harder et al., 2016; Langs et al., 2021) for the period 2017-Sep-01 06:00:00 to 2018-Aug-30 06:00:00 averaged to a one-hour temporal interval. The CRHO stations used for the evaluation are described in Table 1 and their

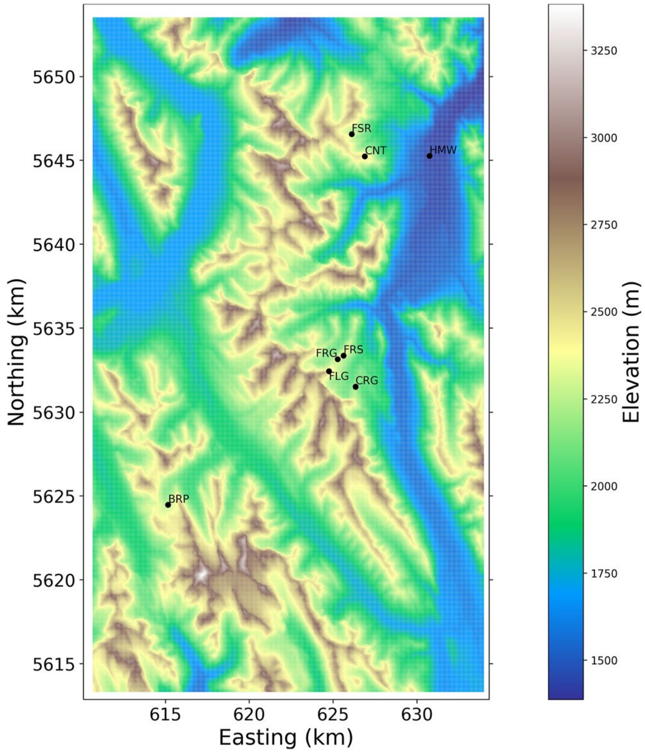

Figure 4. DEM of the study area located in the Canadian Rockies, west of Calgary. Canadian Rockies Hydrological Observatory stations used for this study are summarized in Table 1 and are shown as points. The *x* and *y* axes are UTM 11N metres.

location is shown on Figure 4. These stations range from low elevation valley sites (e.g., Hay Meadow; 1,492 m) to high elevation ridge lines (e.g., Centennial Ridge; 2,470 m). The hourly data were compiled from quality controlled 15-min observations using the methodology detailed in Fang et al. (2019). For the study herein, only open and exposed sites are considered (see model configuration for more details). The Topographic Position Index (TPI), following Winstral et al. (2017), of each station is listed. TPI values of >150 m were taken as indicative of upper slopes and ridge lines.

3.4. Input Wind Fields

Output from the Environment and Climate Change Canada High-Resolution Deterministic System (HRDPS; Milbrandt et al., 2016) was used as input forcing fields for all simulations. These were selected due to their previous use, availability, and suitability over the study area. The HRDPS data consisted of hourly wind speed and direction at 2.5 km grid spacing taken at 40 m above the surface. Successive HRDPS forecasts were combined into a temporally continuous data set as done in Vionnet et al. (2021). Near-surface 2-m winds were estimated using the log-law relationship and a constant $z_0 = 0.01$ m. For all model runs, the period 2017-Sep-01 06:00:00 to 2018-Aug-30 06:00:00 was simulated at a one-hour temporal timestep for a total of 8,712 timesteps.

3.5. Model Configuration

3.5.1. Windmapper

Windmapper was used to produce a 50 m wind field library for use with the Canadian Hydrological Model (CHM) (Marsh et al., 2020) to downscale the HRDPS output across a section of the Canadian Rockies, described in the previous section. However, CHM uses an unstructured mesh that may optionally have a variable resolution across the domain. Detailed in Marsh et al. (2020), this variable resolution, triangular unstructured mesh is generated so-as to minimize an error function (e.g., Root Mean Squared Error; RMSE) between the generated triangles and an underlying raster, such as topography. Multiple error functions and input rasters can be used so-as to minimize the error simultaneously. Thus, multiple landscape data such as vegetation and topography can be used to ensure that important surface heterogeneity is persevered as required. This is done by using smaller triangles. Areas with less heterogeneity can be represented using larger triangles, thus reducing the total number of computational elements. In practice, this strategy can reduce the total number of computational elements by 50%–90% in complex terrain (Marsh et al., 2019, 2020; Vionnet et al., 2021) while preserving simulation fidelity.

Table 1
List of Canadian Rockies Hydrological Observatory Meteorological Stations Used

Station name	Abbreviation	Latitude (°)	Longitude (°)	Elevation (m)	TPI (m)
Burstall Pass	BRP	50.7606	−115.3671	2,260	−93
Hay Meadow	HMW	50.9441	−115.1389	1,492	−34
Fisera Ridge	FSR	50.9568	−115.2044	2,325	−6
Canadian Ridge	CRG	50.8215	−115.2063	2,211	74
Fortress Ridge	FRG	50.8364	−115.2209	2,327	100
Fortress Ridge South	FRS	50.8382	−115.2158	2,306	135
Fortress Ledge	FLG	50.8299	−115.2284	2,565	217
Centennial Ridge	CNT	50.9447	−115.1937	2,470	248

Note. Topographic position index (TPI) >150 m classifies upper slopes and ridges. These areas are considered more wind exposed.

10.1029/2022WR032683

When discussing the resolution of a triangular mesh, it is useful to compare the triangle area to compare to raster grid cells. For example, a "50 m raster" is typically understood to refer to a raster whose cell size is 50 × 50 m (2,500 m^2). For a triangular mesh, a "50 m mesh" would be also understood as having a mesh with triangles of area 2,500 m^2.

A baseline Windmapper CHM configuration was created following the snow-drift permitting resolution in Vionnet et al. (2021) of a 50–250 m variable resolution mesh. This mesh was created using the Mesher tool (Marsh et al., 2018) using the 30 m SRTM DEM as input. The Windmapper configuration is as follows: a 50 m Windmapper spatial resolution, an averaging area (L) of 1,000 m (in agreement with the finding of Barcons et al. (2018) in complex terrain), and 24 look-up maps. In all cases including the uncertainty analysis, lee-side detection via the Sx parameter was enabled with a critical slope of 20°.

For each time-step the HRDPS wind speed and wind direction from the four nearest HRDPS cells to a given computational cell were converted to zonal u and meridional v components. These u and v components were then spatially interpolated to the given triangle using the inverse distance weighting (IDW) method. The wind direction was reconstructed from the interpolated zonal u and v components and the appropriate per-triangle wind speed map was selected.

3.5.2. MicroMet

A frequently used terrain-based algorithm for estimating mechanical impacts of terrain on wind fields is the MicroMet approach of Liston and Elder (2006) that provides the impact of terrain on the speed via terrain curvatures and direction of wind via the parameterizations of Ryan (1977). Herein an implementation of the MicroMet (Liston & Elder, 2006) terrain curvature algorithm adapted for use with the unstructured meshes of CHM was used.

In brief, the MicroMet algorithm works by computing a wind weight factor (W_w) that weights the topographic slope in the wind direction (Ω_s) and the terrain curvature (Ω_c) such that

$$W_w = 1 + \gamma_s \Omega_s + \gamma_c \Omega_c \tag{9}$$

where γ_s and γ_c are the slope and curvature weights. The definition of the topographic slope in the wind direction and the terrain curvature are given in Liston and Elder (2006). Default values of γ_c and γ_s are 0.5 and 0.5, giving equal weights to both slope and curvature (Liston & Elder, 2006). Following Pohl et al. (2006), the weights used here are $\gamma_c = 3$ and $\gamma_s = 1$. These values were determined by Pohl et al. (2006) by calibrating against the MS3DJH/3R (Walmsley et al., 1986) windflow model.

3.5.3. WindNinja

WindNinja was run using the HRDPS atmospheric forcing, as described above, to provide a direct downscaling of the HRDPS wind field over the study area. This method uses the option in Wind Ninja proposed by Wagenbrenner et al. (2016) to downscale Weather Research and Forecasting Model (WRF) wind field in complex terrain. It requires that the atmospheric forcing be in a Lambert Conformal Conic projection. Therefore, the HRDPS data were re-gridded from the original rotated model grid to the Canadian Lambert Conformal Conic. The re-gridding was done using the pyresample (Nielsen, 2013) Python package with an output extent, number of cells, and spatial resolution that matches that of the input HRDPS. The input surface elevation was described by the SRTM DEM at 30 m resolution, re-gridded to a 50 m raster mesh.

The HRDPS wind speed and wind direction from the four nearest HRDPS cells to a WindNinja cell were converted to zonal u and meridional v components. These were then spatially interpolated via bilinear interpolation. WindNinja was configured to run in the mass-conserving mode with a 50 m mesh resolution using the internal "grass" vegetation surface. No diurnal winds were considered. Model outputs were every 1 hr, corresponding every HRDPS timestep.

3.5.4. Extraction of Points

To compare the model output to the point-scale meteorological station observations, the corresponding computational cells needed to be extracted from the spatial model. For the Windmapper and MicroMet implementations in CHM, the triangle that fully contained the latitude/longitude of each station was selected. This was done during the CHM runtime. For WindNinja, the nearest raster cell was selected in post processing.

Table 2
List of Values for Each Uncertainty Analysis Parameter

L (m)	WindNinja resolution (m)	Number of directions ()	CHM mesh
500	50	4	Variable (50–250 m)
1,000	150	8	Constant (50 m)
1,500	250	12	
		24	
		36	

Note. A 108 total combinations were run.

This approach has an obvious scale conflict, where, at a minimum, a 50 × 50 m cell, and potentially larger triangle is being taken as representative of a point observation. Despite this, no sub-grid modification was done, and the points were taken as-is. There was no optimization of point locations to improve output.

3.6. Uncertainty Analysis

An uncertainty analysis was performed on the three parameters that control the wind field generation in Windmapper: (a) the area over which the speedup averaging is done (L in Equation 1); (b) the impact of fine and coarse spatial resolutions of the WindNinja simulation to generate the wind field library; (c) the number of directions in the Windmapper library; and (d) the impact of a variable resolution mesh in CHM on the application of Windmapper. The values for these parameters are listed in Table 2. A total of 108 combinations were run. The L_{avg} distance values (m; over which the speedup averaging is done (L in Equation 1)) were chosen as they are thought to represent the local topography's length scale influence on wind patterns. Further, these ranges match previous work (Barcons et al., 2018; Marsh et al., 2019; Vionnet et al., 2021). The impact of a variable resolution mesh in CHM on the application of Windmapper is investigated as such a variable resolution mesh has not used with wind library algorithms previously. For this uncertainty analysis two CHM unstructured meshes are used. One with a constant 50 m triangle resolution, and one with a variable resolution with a minimum triangle area of 50 m and a maximum of 250 m with a maximum error of 15 m RMSE.

This uncertainty analysis compared the CHM Windmapper output compared to the WindNinja output at the computational cells that correspond to the observations described above, listed in Table 1.

3.7. Evaluation

Two evaluations are done: a point-scale comparison against observations and a spatial comparison between Windmapper and the WindNinja simulation.

3.7.1. Evaluation 1

The extracted point-scale outputs from Windmapper and MicroMet implementations in CHM were compared to the observations at the above-described meteorological stations. The Root Mean Squared Error (RMSE) and bias were used to quantify the error between the model and observations. This was done for the wind speed and wind direction.

3.7.2. Evaluation 2

The Windmapper output from CHM (using the variable resolution mesh) was rasterized to a 50 × 50 m raster, corresponding to the WindNinja mesh resolution. This rasterisation was done via the GDAL rasterisation algorithm (GDAL/OGR contributors, 2020). In brief, this algorithm takes the triangle geometry in conjunction with a desired raster geometry and resolves which raster cells correspond to each triangle. If two triangles share an output cell, an overwrite is used. Then, this CHM-derived raster was compared to the WindNinja output where the RMSE and bias were computed for each raster cell. The Sx parameterization as not enabled for WindMapper for ease of comparison with WindNinja.

To quantify how the differences between the two models are impacted by topographic location, the TPI was calculated following Winstral et al. (2017). TPI values of >150 m were taken as indicative of upper slopes and ridge lines, and all other TPI values were assigned an "other" designation for the analysis. Locations of TPI <0 are not considered as these locations (in this domain) are heavily forested (in reality). As the impacts of the forest on windfields is not considered here, the use of a forested locations would be a major source of uncertainty.

10.1029/2022WR032683

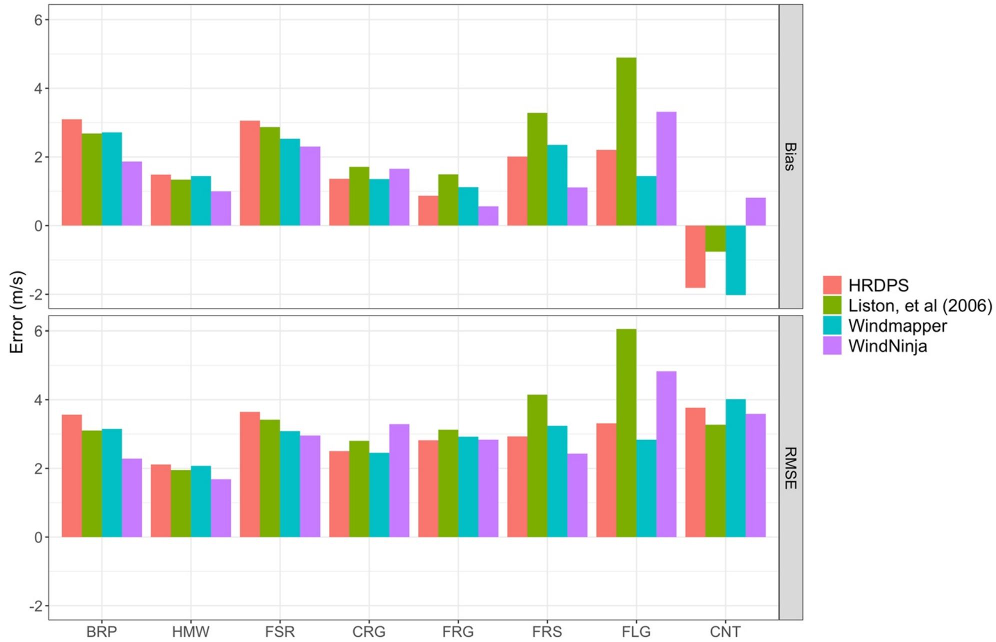

Figure 5. Mean bias, Model-WindNinja, (m · s^{-1}; top panel) and RMSE (m · s^{-1}; bottom panel) of the wind magnitude compared to observations for the non-downscaled HRDPS, the Liston and Elder (2006) method, Windmapper (this study), and the standalone WindNinja model. The error metric is computed at the specified observation points Table 1.

3.8. Benchmarking

To quantify the computational resources required for CHM and WindNinja, the CHM and WindNinja simulations were performed on Compute Canada "Graham" cluster. Each Graham node is comprised of 2 × 16-core Intel E5-2683 v4 Broadwell at 2.1 GHz with 125 GB RAM.

Although CHM supports the Message Passing Interface (MPI) for distributed computing, only a single node was required for the CHM run. A total of 32 threads via OpenMP were used.

The parallel scheme in WindNinja is exclusively via OpenMP where each timestep is run in parallel. Due to the more compute-intensive aspect of WindNinja, 242 nodes were used, each with 16 threads utilized. The low thread utilization was due to memory constraints.

4. Results

4.1. Point Observation Comparison

The Windmapper baseline configuration (teal) was compared to the MicroMet implementation (green) in CHM, the non-terrain corrected, non-downscaled HRDPS output (red), and the WindNinja (purple) output at the observed stations. This is shown in Figure 5 and Figure 6 for the windspeed and wind direction respectively. The top panel is the bias and the bottom panel is the RMSE. The observed meteorological station short-codes (see Table 1 for full names) are on the *x*-axis. The stations are arranged in order of increasing TPI, indicating increased wind exposure.

For the wind speed comparison shown in Figure 5, for all stations except Centennial Ridge (CNT), there was a positive bias (top panel) from the non-downscaled HRDPS, indicating an over estimation of windspeed. At the three low-TPI sites (Burstall Pass (BRP), Hay Meadow (HMW), Fisera Ridge (FSR)) the downscaling approaches all reduced this positive bias. At the Canadian Ridge (CRG) site, an exposed ridge, Windmapper provided limited benefit versus the HRDPS speed, however both the MicroMet and WindNinja approaches increased the bias versus the baseline HRDPS (1.71 and 1.65 m · s^{-1} vs. m · s^{-1}, respectively). At the increasingly exposed ridges of Fortress Ridge (FRG), Fortress Ridge South (FRS), and Fortress Ledge (FLG), the MicroMet method had the largest positive bias (1.49, 3.28, 5.0 m · s^{-1}, respectively). At these sites, Windmapper had a bias of 1.35, 2.35,

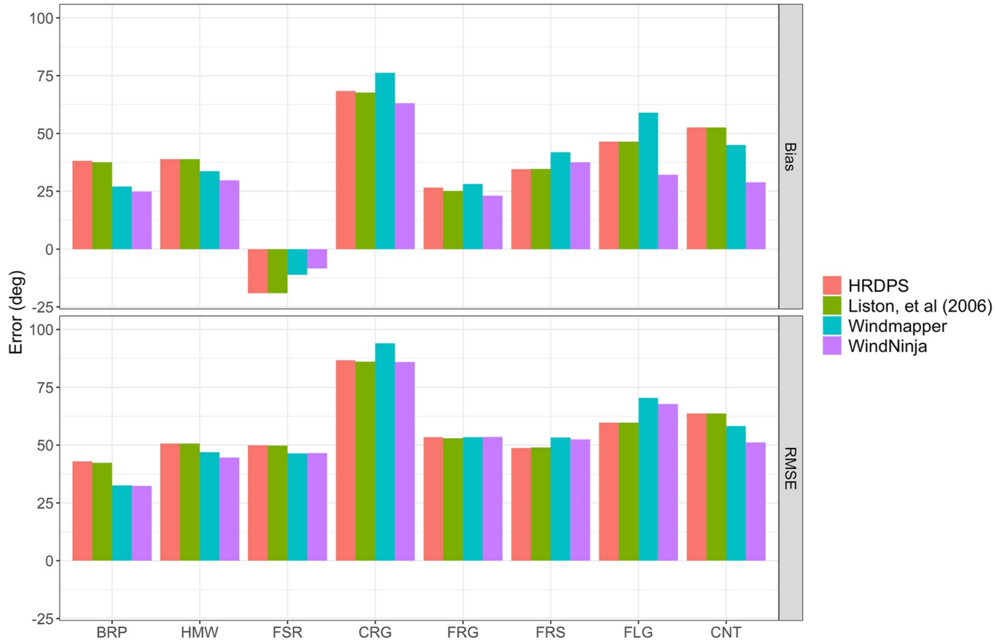

Figure 6. Mean bias, Model-WindNinja, (°; top panel) and RMSE (°; bottom panel) of the wind direction compared to observations for the non-downscaled HRDPS, the Liston and Elder (2006) method, Windmapper (this study), and the standalone WindNinja model. The error metric is computed at the specified observation points Table 1.

and 1.45 $\mathrm{m \cdot s^{-1}}$, respectively. The Windmapper approach tended to have a similar bias as the HRDPS, and the stand alone WindNinja had consistently the lowest bias. However, at the FLG site, both MicroMet and WindNinja dramatically overestimates the windspeed (bias of 4.90 and 3.32 $\mathrm{m \cdot s^{-1}}$, respectively). The CNT site had the HRDPS, MicroMet, and Windmapper with a negative bias, whereas WindNinja had a positive bias. At the CNT ridge, Micromet had the lowest bias (0.76 $\mathrm{m \cdot s^{-1}}$). For the majority of the sites, Windmapper had a lower bias than the terrain curvature and non-downscaled HRDPS methods. The FLG site was unique in that it was the only site where WindNinja performed the worst.

Similar results follow for the RMSE of windspeed. At the less exposed stations (BRP, HMW), WindNinja had the lowest RMSE. Windmapper was quite close or slightly better than the MicroMet implementation (difference of $\approx 0.05\,\mathrm{m \cdot s^{-1}}$). Along the more exposed stations such as FRS and FLG, Windmapper had a substantially lower RMSE than the MicroMet implementation (3.24 and 2.83 $\mathrm{m \cdot s^{-1}}$ vs. 4.14 and 6.05 $\mathrm{m \cdot s^{-1}}$, respectively).

The bias (top panel) and RMSE (bottom panel) for wind direction are shown in Figure 6. At the less exposed sites of BRP and HMW the limited terrain correction of MicroMet produced a result almost identical to that of the underlying HRDPS value (37.55° and 38.91° vs. 38.16° and 38.91°, respectively). Windmapper and WindNinja subsequently reduced this bias by better accounting for valley bottom channeling. The CRG stations had the largest bias for the Windmapper method (76.20°). The more exposed ride lines of FRG, FRS and FLG had progressively more bias for the Windmapper method, whereas WindNinja had decreasing bias. At the most exposed CNT station Windmapper out-performed the MicroMet code (45.10° vs. 52.61° respectively). The trend of limited terrain correction in the MicroMet method was reflected with an almost unchanged bias to that of the HRDPS simulation.

Similar results for the RMSE of the direction are seen with the MicroMet code performing almost identically to that of the HRPDS model. For example, at the valley sites BRP and HMW this was 42.26° and 50.68° versus 42.93° and 50.68° respectively. At the low elevation valley sites of BRP and HMW, the RMSE of Windmapper and WindNinja are decreased versus the HRDPS value as they accounted for the valley channeling.

10.1029/2022WR032683

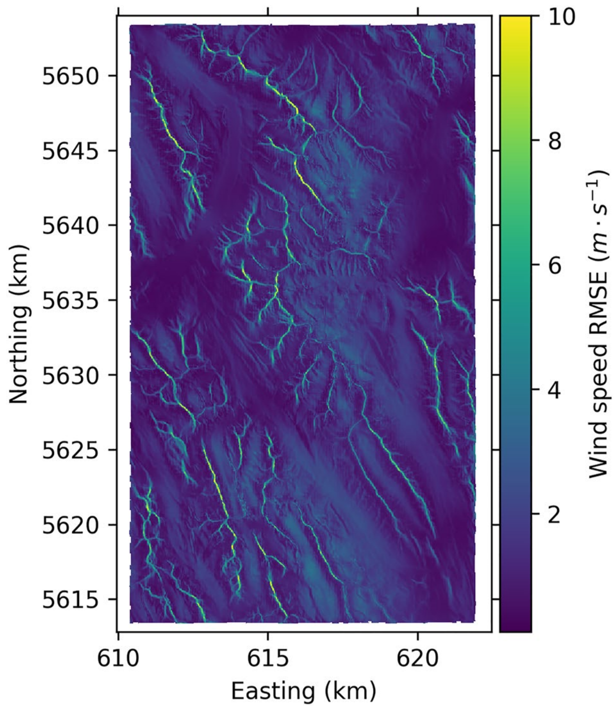

Figure 7. RMSE ($\mathrm{m \cdot s^{-1}}$) between Windmapper and the standalone WindNinja of the wind magnitude. The RMSE is evaluated at each grid cell for the entire simulation period. The *x* and *y* axes are UTM 11N metres.

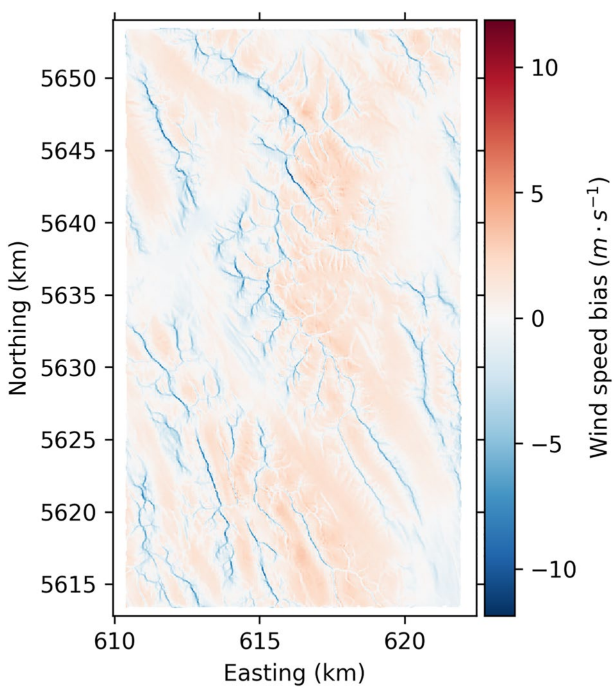

Figure 8. Bias, Windmapper-WindNinja, ($\mathrm{m \cdot s^{-1}}$) between Windmapper and the standalone WindNinja of the wind magnitude. The bias is evaluated at each grid cell for the entire simulation period. The *x* and *y* axes are UTM 11N metres.

4.2. Spatial Model-Model Comparison

4.2.1. Wind Speed

To quantify the spatial variability for the entire simulation period in how the Windmapper simplification differs from WindNinja, the RMSE and bias of wind speed and direction was computed on a per-cell basis over the entire simulation period. The RMSE of the wind speed is shown in Figure 7 and bias in Figure 8. The largest differences between Windmapper and WindNinja were along the ridges, with the valleys having low RMSE (typically $<3\ \mathrm{m \cdot s^{-1}}$). The bias is near zero for the majority of the valleys and was generally $>-5\ \mathrm{m \cdot s^{-1}}$ on the ridges, indicating an under estimation of windspeed compared to WindNinja. For RMSE the range was 0.2–14.8 $\mathrm{m \cdot s^{-1}}$, the mean was 1.4 $\mathrm{m \cdot s^{-1}}$, the first quartile was 0.8 $\mathrm{m \cdot s^{-1}}$, and the third quartile was 1.8 $\mathrm{m \cdot s^{-1}}$. For the bias, the range was −11.9 to 4.6 $\mathrm{m \cdot s^{-1}}$, the mean was 0.28 $\mathrm{m \cdot s^{-1}}$, the first quartile was −0.25 $\mathrm{m \cdot s^{-1}}$, and the third quartile was 1.1 $\mathrm{m \cdot s^{-1}}$.

Shown in Figure 9 is the distribution RMSE and bias of wind speed, shown as a function of TPI, allowing for the identification of where the difference occurs. Upper slopes and ridges (TPI >150 m; teal) had the majority of large differences (left panel, RMSE) and these differences are generally an under estimation of wind speed (right panel, bais).

Wind Direction The same procedure that was done for the spatial wind speed comparison was done for the wind direction. The spatial map of RMSE and bias for wind direction are not shown and are summarized as follows. These RMSE and bias values are shown as a histogram in Figure 10. The range of the direction RMSE is 16.7°–225°, the mean is 50.9°, the first quartile is 39.7°, and the third quartile is 58.2°. For the direction bias, the range is 0°–142.7°, the mean is 10.4°, the first quartile is 4.3°, and the third quartile is 14.4°. Unlike the windspeed, the largest biases in direction are not clearly dominated by the upper slopes and ridges (TPI >150m; teal).

The qualitative comparison of streamlines is given in Figure 11. The first timestep was chosen due to the relatively uniform flow from the North-West as predicted by HRDPS thus providing a straightforward analysis example. The streamline plot displays the 2D vector field of the windflow for: the reference WindNinja simulation (left); the WindMapper approximation (centre); and the Ryan (1977) algorithm as described by Liston et al. (2016) and implemented on an unstructured mesh for use in CHM (right). For visualization clarity, stream lines are allowed to terminate if they come too close to another streamline. Arrows show the direction of flow.

Broadly WindMapper shows a closer match to the reference WindNinja flows than the Ryan/Liston (RL) method. Limited valley channelling is observed in the RL plot, with the streamlines broadly flowing the main HRDPS circulation flow. In contrast, the WindMapper flows show many of the valley channeling i.e., observed in the reference WindNinja flows. As an example, the complex flow observed at $y = 616$ km and $x = 5{,}640$ km in the WindNinja flows are well approximated in the WindMapper flows. Overall, WindMapper has close qualitative agreement with the WindNinja flows.

4.3. Uncertainty Analysis

An uncertainty analysis was performed on the four parameters that control the wind field generation in Windmapper and CHM: (a) the area over which

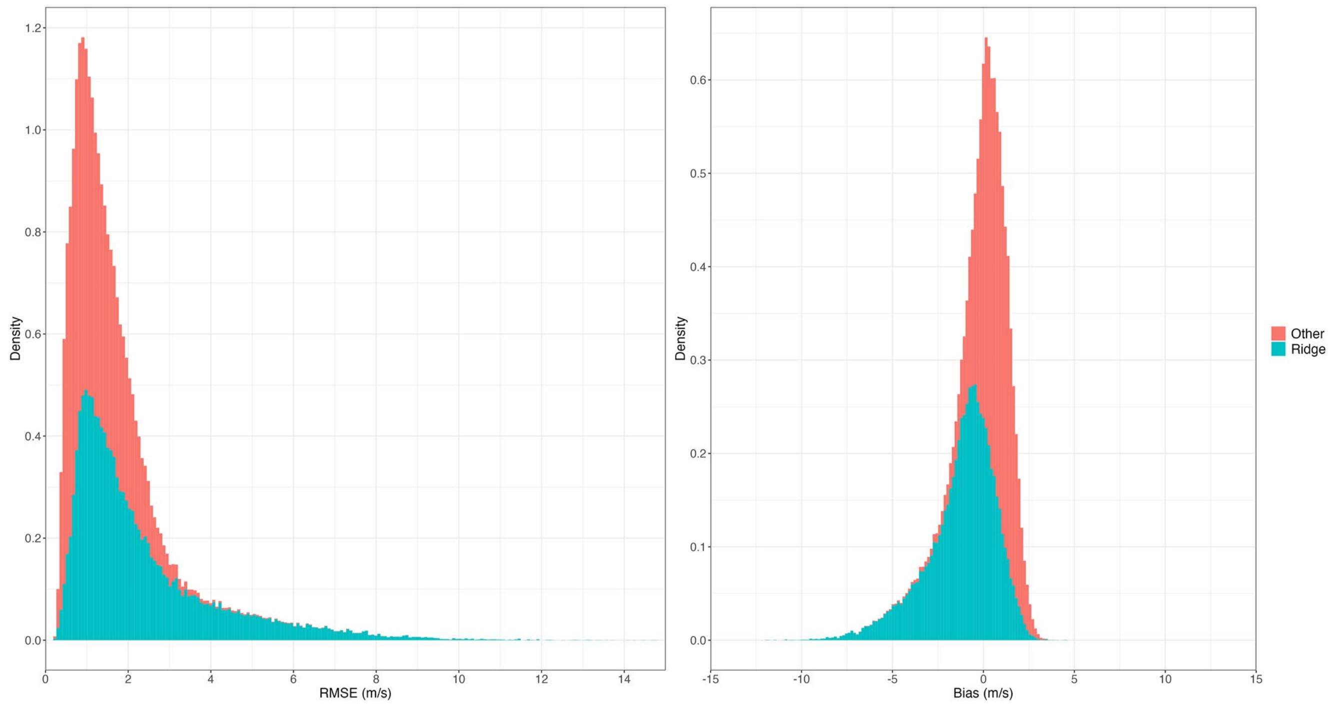

Figure 9. Histogram of RMSE (m · s^{-1}) and bias, Windmapper-WindNinja, (m · s^{-1}) between Windmapper and the standalone WindNinja of the wind speed for upper slopes and ridges (TPI>150m; teal) and all other locations (red).

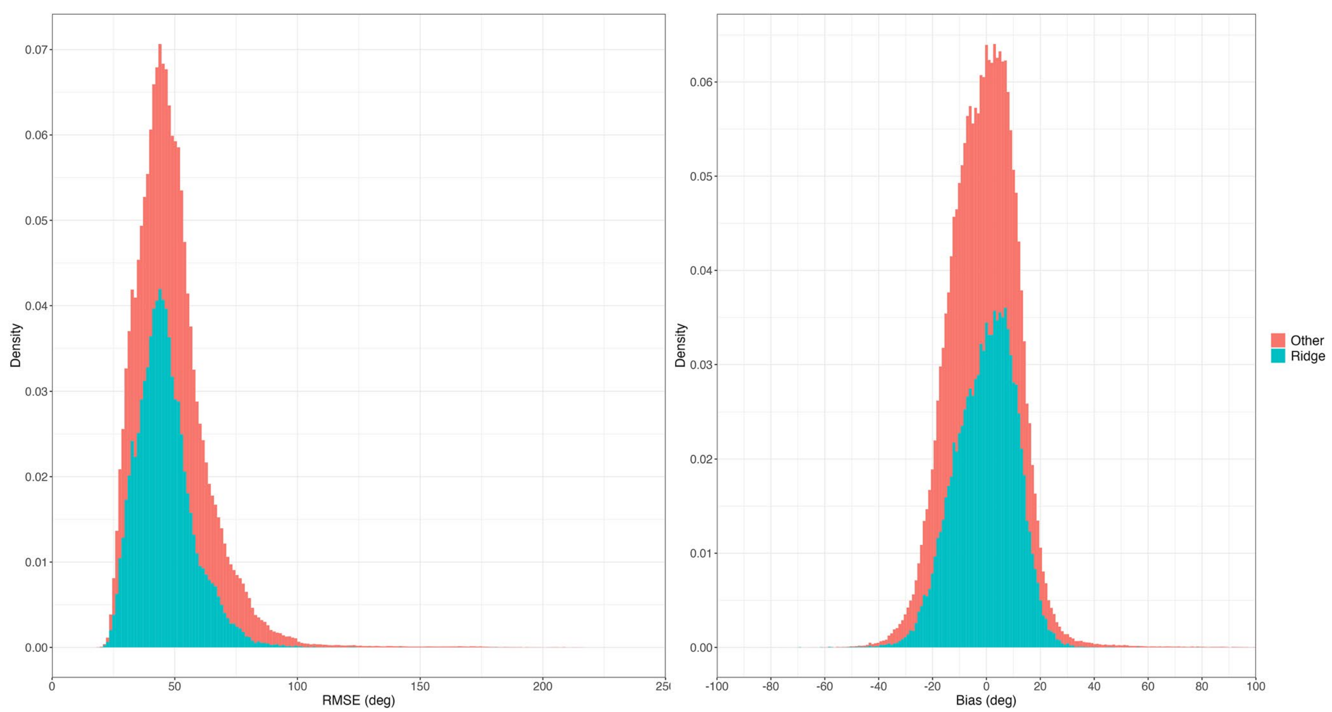

Figure 10. Histogram of RMSE (°) and bias, Windmapper-WindNinja (°) between Windmapper and WindNinja of the wind direction for upper slopes and ridges (TPI>150m) and all other locations.

10.1029/2022WR032683

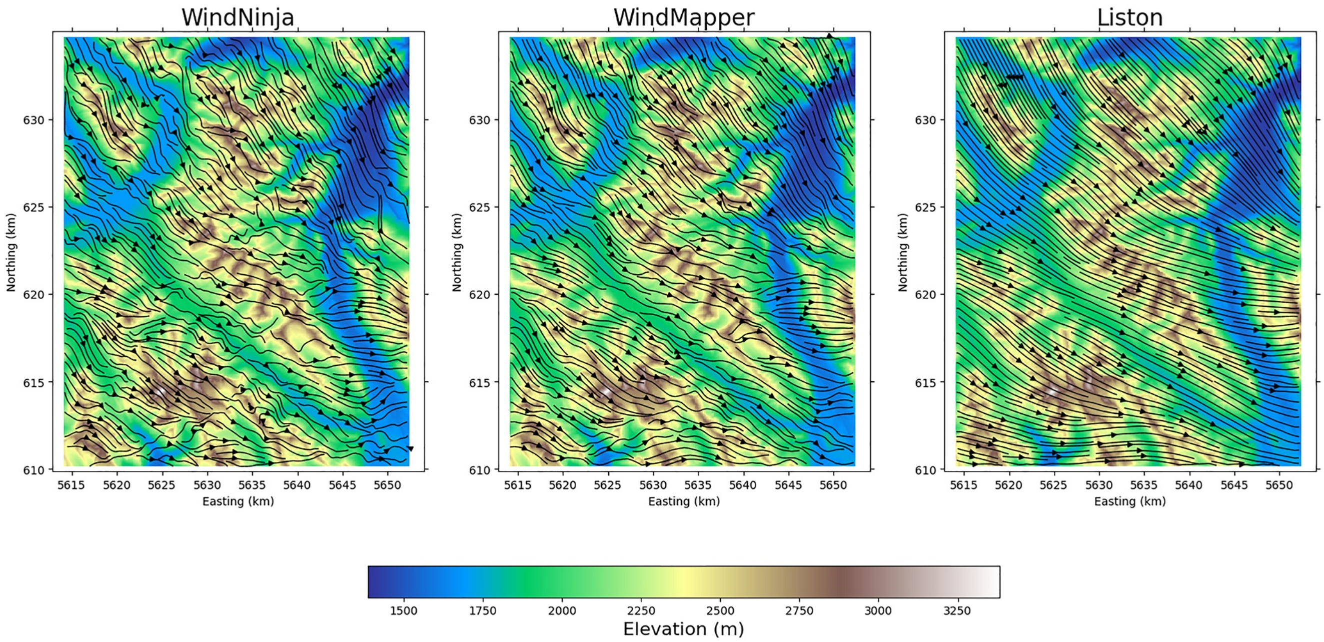

Figure 11. Qualitative comparison between the streamlines of WindNinja reference solution (left), WindMapper approximation (centre), and Ryan/Liston method (right).

the speedup averaging is done (L in Equation 1); (b) the spatial resolution of the WindNinja simulation; (c) the number of directions in the Windmapper library; and (d) the impact of a variable resolution mesh in CHM on the application of Windmapper. These results are summarized as RMSE versus observations at the sites listed in Table 1, and are shown in Figures 12 and 13 for the wind speed and wind direction respectively.

There was substantial improvement in wind speed RMSE when the number of wind field maps are increased; however past 12-maps there is negligible improvement and no improvement past 24. This was most pronounced at the higher TPI (i.e., exposed) sites. At the valley site of HMW, there was no change regardless of the number of maps used.

As the averaging area increased there tended to be a decrease in RMSE of wind speed at the low TPI and high TPI sites. Further, the spread between the variable resolution and fixed resolution meshes increased as the averaging area was increased. The higher resolution WindNinja runs (50 m) tended to produce lower RMSE values across all stations, and this was most pronounced at the most exposed sites.

At the low TPI sites, ending at the FRS site, the fixed and variable resolution meshes had similar RMSE values, with the variable resolution tending to have slightly lower RMSE values. At the more exposed sites, FLG and CNT, the variable resolution mesh performs less well than the fixed resolution mesh. Overall, there was limited degradation in simulation performance using the variable resolution mesh.

When evaluated at the point scale, the wind direction was the least susceptible to increasing the number of maps with negligible improvements after 12 maps. However, the increase from 4 to 8, especially at the exposed sites such as FLG was pronounced. Overall, there was limited difference between the variable and fixed resolution meshes, and nor was there much impact from various WindNinja resolutions.

4.4. Computational Costs

The variable resolution CHM mesh with 24 Windmapper directions took a wall-clock time of 16380s (4 hr 33 min) to run for the 8,712 timesteps.

The standalone WindNinja simulation with a 50 m mesh took approximately 2 hr per-node. Therefore, in order to compare to the CHM wall-clock time, each nodes total wall clock time was summed. Thus, the single-node equivalent wall-clock time was 1626759s (18 days 19:52:39).

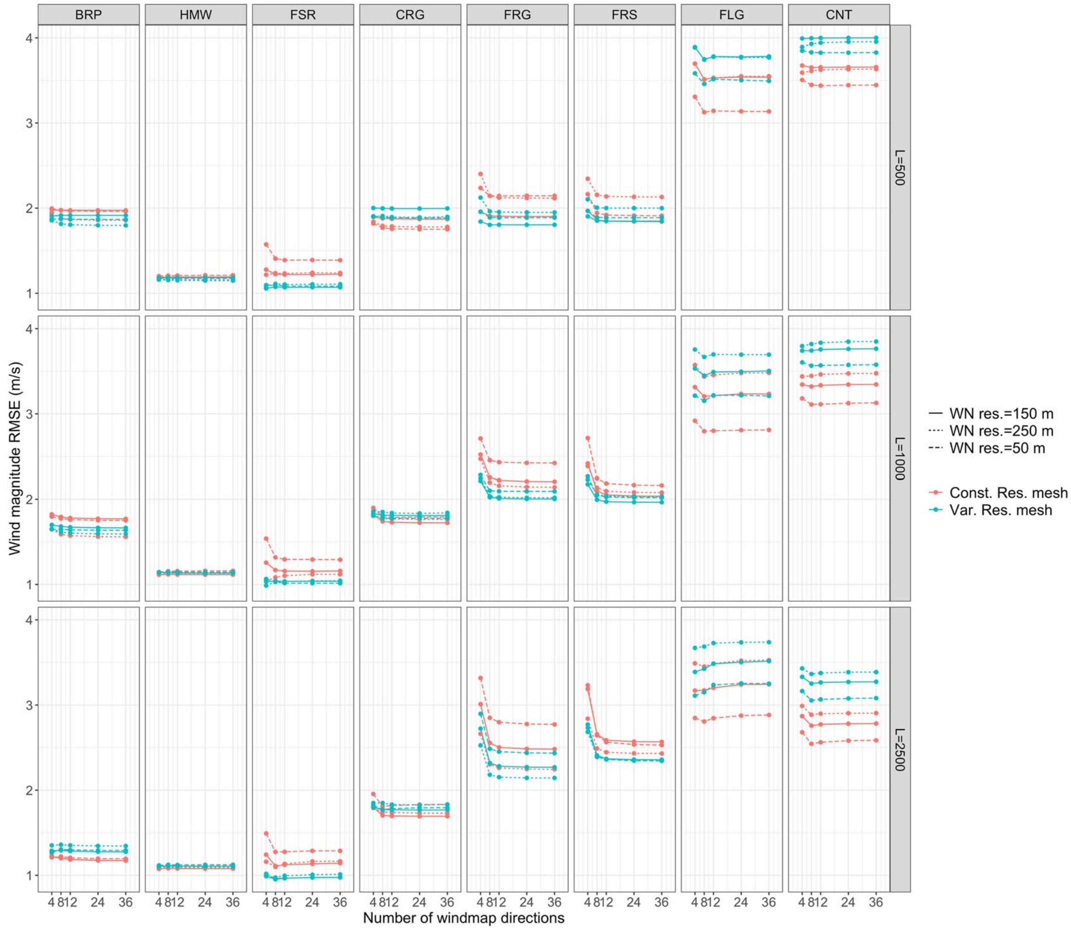

Figure 12. Uncertainty analysis for the application of Windmapper in the Canadian Hydrological Model (CHM) evaluated at the observation sites listed in Table 1. The line type corresponds to the WindNinja (WN) mesh resolution (res.) used as input to Windmapper, and the colours to either the variable (var.) or fixed (const.) resolution mesh in CHM, the vertical panels to the L_{avg} distance (m; over which the speedup averaging is done (L in Equation 1)), and the x-axis to the number of wind field maps used in Windmapper.

5. Discussion

Incorporating the mechanical terrain effects on wind flow in mountains terrain is a difficult and computationally expensive task. In this work, a model simplification approach was presented that expanded the work of Essery et al. (1999) and Barcons et al. (2018). This previous work used a CFD windflow model to build a library of wind flow maps which were used to perturb input wind speeds to account for the terrain effects. This type of approach allows for massively reduced computational burdens at the cost of decreased accuracy.

The Windmapper approach detailed herein showed generally consistent improvements against existing methods such as the terrain curvature method of Liston and Elder (2006) for both wind speed and direction. The improvement versus the MicroMet algorithm is especially pronounced for perturbations to the wind direction where almost no correction was done from the underlying HRDPS wind field. The limitation in direction perturbation via Ryan (1977) has been documented elsewhere. Musselman et al. (2015) identified that despite generally accurate wind speed estimates along ridges, the resulting wind field from terrain curvature methods such as Liston and Elder (2006) and Ryan (1977) were insufficient for use with advection equations such as blowing snow transport and redistribution. The wind library approach detailed here has been used successfully with a blowing snow model (Marsh et al., 2019; Vionnet et al., 2021) and as such appears to avoid the terrain curvature limitations for derivative calculations on the windflow. This is in agreement with Essery et al. (1999) who used a similar approach with a simple blowing snow model, also based on the Prairie Blowing Snow Model (PBSM) (Pomeroy & Li, 2000). There is thus some evidence that wind library approaches improve upon the terrain curvature methods for advec-

10.1029/2022WR032683

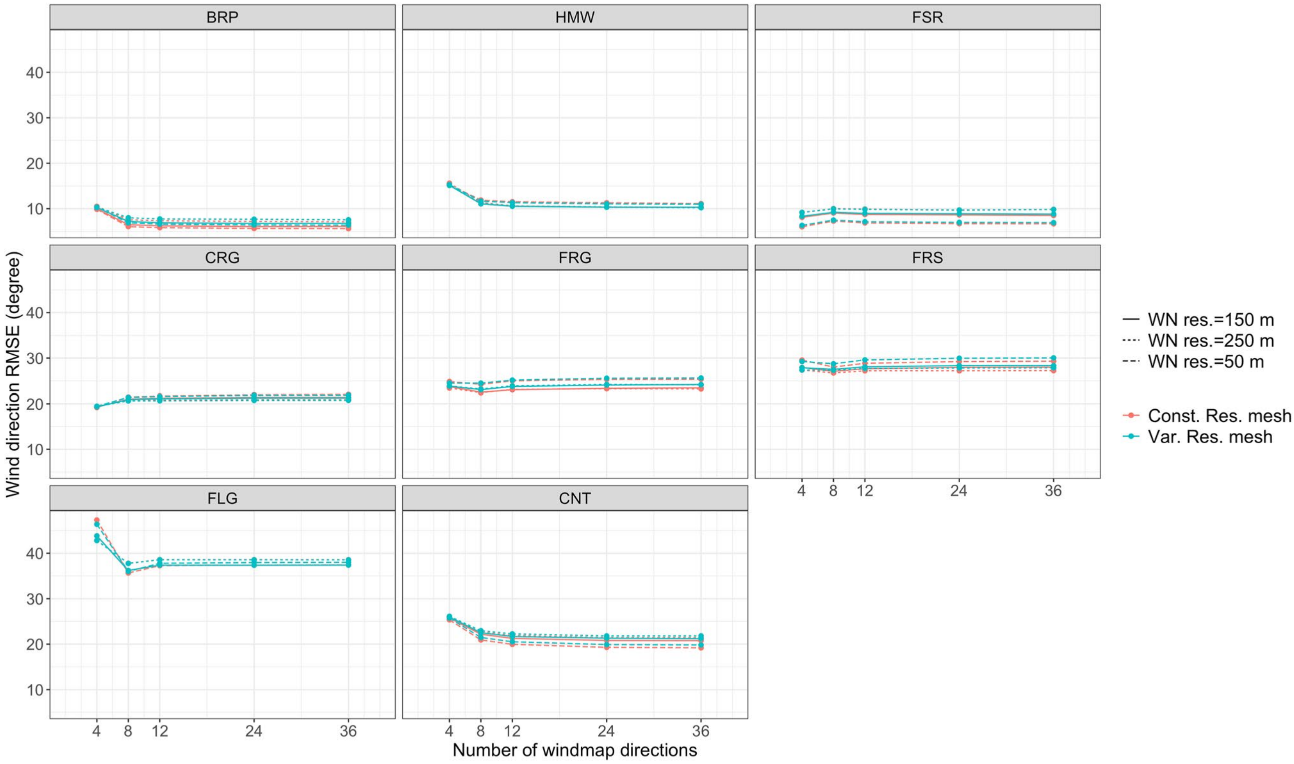

Figure 13. Uncertainty analysis for the application of Windmapper in the Canadian Hydrological Model (CHM). The line type corresponds to the WindNinja (WN) mesh resolution (Res.) used as input to Windmapper, and the colours to either the variable (Var.) or fixed (Const.) resolution mesh in CHM, and the *x*-axis to the number of wind field maps used in Windmapper. No L_{avg} distance is used for direction correction (as the direction is directly obtained from the map library) and so is not shown here.

tion problems. Lastly, it was shown that the WindNinja simulations overall had reasonable direction agreement with observations. However, there is a systematic over estimation in windspeed along the ridges.

Because observations of wind velocity are spatially sparse, evaluating the spatial heterogeneity of a wind model is difficult. The comparison of Windmapper to point-scale observations had a scale mismatch where computational cells (i.e., an area average) were compared to point-scale observations. This is further complicated with a variable resolution mesh, such as that used herein. The variable resolution meshes are a key aspect of preserving small scale features while allowing for large spatial extents to be represented in an explicitly distributed manner. However, it means that in such a comparison, the computational element containing the point observation may be more off-ridge than in reality, and thus results in a somewhat biased answer. This is likely the case with the CNT station reported herein as it was observed the triangle was slightly in the lee instead of exactly on the ridge. Overall, the ability of a wind library approach to succeed is dependent upon (a) the accuracy in input wind field; (b) the ability of the underlying CFD model to reproduce micro-topographic flows; and (c) the accuracy in the model simplification. The results here showed that point-scale results versus observations are highly dependent upon the skill of the HRDPS forecast. There is no way to completely compensate via downscaling for an incorrect HRDPS prediction. Although not explored here due to being out of scope, further work should investigate how the performance in the wind direction is correlate with wind intensity, for example, strong synoptic forcing. Indeed, one might expect Windmapper to perform better in these conditions. When the synoptic forcing is weaker, thermal effects (e.g., slope wind and thermal breeze) may be more important and will influence the observed wind direction whereas Windmapper does not account for these diurnal thermal effects.

When Windmapper was compared spatially to WindNinja, the Windmapper approximation to the standalone WindNinja simulation has a third quartile RMSE of 1.9 $\mathrm{m \cdot s^{-1}}$. This error magnitude is well within reported uncertainty ranges for wind observations, for example, Winstral et al. (2009) and Raleigh et al. (2015) of $\pm 3.0\ \mathrm{m \cdot s^{-1}}$. The wind direction had a third quartile error of 60.23°. This suggests there is further improvement to how Windmapper treats direction. Although the Windmapper method does improve upon the terrain curvature methods direction estimate, it is not as accurate as the standalone CFD model.

10.1029/2022WR032683

A large limitation with the Windmapper approach is with respect to flow separation and lee-side recirculation. The mass conserving version of WindNinja does not exhibit these behaviors (Forthofer et al., 2014; Wagenbrenner et al., 2016, 2019). This difficulty is due to the absence of a momentum equation in the mass-conserving version of the WindNinja flow simulation (Forthofer et al., 2014). Previous attempts by the authors to run the momentum conserving version of WindNinja, along with other CFD models proved to be numerically unstable over this region. Although updated versions of the WindNinja code may have fixed these problems (Wagenbrenner, per. comms), the momentum version of the model has not been extensively tested in this region nor with application to advection-transport models, for example, Marsh et al. (2020) and Vionnet et al. (2021). Therefore, Windmapper can be considered a first version of an easily applicable code that can be augmented with more complex and hopefully accurate models in the future. The development of leeward recirculation, although quite important, may not be possible with the Windmapper approach in its current form. Development of such a feature may require tracking multiple up-wind cells so-as to determine flow reversal. This should be addressed in future work and is out of scope of the current implementation.

The uncertainty analysis presented here demonstrated limited improvement in predictions at a point scale with more than 24 wind maps. This is important as over large spatial extents the addition wind maps can begin to have a large memory requirement. Overall, the Windmapper approach with either fixed or variable resolution meshes were similar, however the ridge-lines were best represented by the higher resolution fixed resolution mesh. However, this difference was small, on the order of approximately 0.5 $\mathrm{m \cdot s^{-1}}$. However, the impact of too large of a L value on distributed advection solutions is pronounced (Vionnet et al., 2021). This is due to averaging-out small-scale topographic impacts on wind velocity. The maximal value of L should be the resolution of the atmospheric model being downscaled as tested by Folch et al. (2017) when applying a preliminary version of the wind downscaling method of Barcons et al. (2018). An optimized version of L can be derived from a sensitivity analysis as done in this study. Further work is still required to adapt this value to the resolution of the mesoscale atmospheric models and to the terrain complexity.

The computational savings of almost 100x between the Windmapper approach and the stand alone WindNinja model is substantial. The wall-clock implications of this translates to a 1-node usage of 4 hr versus 18 days. This is not to disparage the WindNinja code—it is a modern C++ code that avails itself of high-performance computing paradigms. Rather, it is the nature of solving such equations. It should be noted that the mass conserving mode of WindNinja used herein was the simplest form of wind simulation available. The computational costs associated with the momentum conserving approach are larger. Therefore, it is thought that the error introduced by the Windmapper approximation is well constrained by the improvement in wall-clock performance. However, future work should consider using the momentum-conserving approach in WindNinja to produce the wind library.

Lastly, the Windmapper algorithm and code allows for producing the wind library at large spatial extents; extents greater than previously reported by Barcons et al. (2018) or Essery et al. (1999). An example of this is shown in Figure 14 where the Windmapper algorithm was run for 1.3 M $\mathrm{km^2}$ at a 50 m spatial resolution. Such a capacity enables use in large extent models that wish to preserve high-resolution topographic impacts on wind flows. This is a unique aspect of this approach and will hopefully enable large-extent, high-resolution modeling in the future.

6. Conclusions

Near surface wind speeds and directions are a key meteorological input for many hydrological and biological system process models. However, despite this importance, surface observations tend to be spatially sparse and are often not present in key locations such as mountain headwaters are often not present. Distributed models motivate the inclusion of distributed wind fields, often by downscaling numerical prediction output, or by spatially interpolating point observation when available. Incorporating the mechanical terrain effects on wind flow in mountains terrain is a difficult and computationally expensive task. Therefore, there is substantial motivation for computationally efficient methods to estimate near surface winds.

In this work the software tool Windmapper was described. This model simplification allows for efficient downscaling of wind velocities from numerical weather prediction output or from dense observation networks. This approach builds upon the pre-computed wind library approaches of Essery et al. (1999) and Barcons et al. (2018). These pre-computed wind field libraries are used to perturb an input wind field to account for the influence of topographic features on wind speed and direction. New here is a generic software using the WindNinja CFD model that enables application to large spatial extents (millions of $\mathrm{km^2}$), is applicable to unstructured, variable

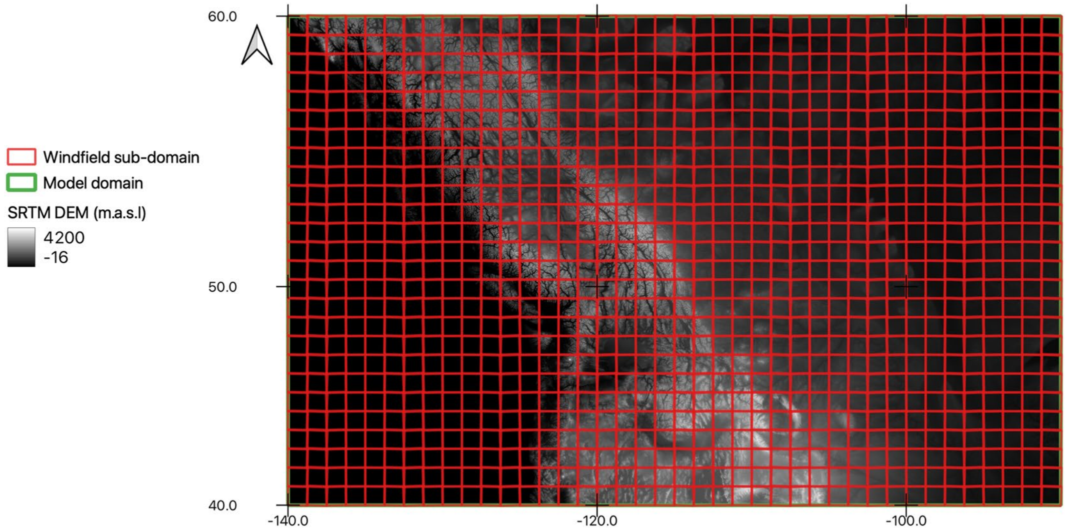

Figure 14. An example of applying Windmapper at a large spatial extent. This example was run for a section of the Canadian Cordillera, an area of 1.3 M km^2. The underlying WindNinja spatial resolution was 50 m. The sub-domains that are stitched together are shown in red.

resolution meshes, incorporates lee-side speed reduction estimates, and that also utilizes the wind library to perturb wind directions. Overall, this approach was shown to have a third quartile error of 1.9 m $\cdot$ s^{-1} versus the standalone CFD model, a value within reported uncertainty bounds for wind observations (Winstral et al., 2009). A third quartile error of 60.23° was also found for wind direction. The wind direction estimates versus observations were better than existing terrain-based estimates however further improvements are warranted. The Windmapper approximation came at a substantial improvement (100x) in computational cost, with the Windmapper approach taking 4.5 hr of wall-clock time whereas the underling CFD simulation took almost 19 days for a year of hourly simulations for an approximately 1,000 km^2 domain.

In summary, the Windmapper approach enables easily generating pre-computed wind libraries for use in land-surface models at both a high spatial resolution and spatial extent. Future work should incorporate the more sophisticated options available in WindNinja (or other CFD model) to further improve the wind field library.

Data Availability Statement

The Windmapper code is open source and available at https://github.com/Chrismarsh/Windmapper. The Canadian Hydrological Model (CHM) code is open source and available at https://github.com/Chrismarsh/CHM. The mesh generation software Mesher is open source and available at https://github.com/Chrismarsh/mesher. The WindNinja code is open source and available at https://github.com/firelab/windninja. The CRHO meteorological data are available at http://giws.usask.ca/meta/. The HRDPS data are available via the Canadian Surface prediction Archive (CaSPAr; https://caspar-data.ca/).

Acknowledgments
The authors would like to acknowledge the WindNinja team including Nathalie Wagenbrenner and Kyle Shannon for their help with various aspects of running WindNinja. The quality-controlled meteorological observations were made possible by Logan Fang (USask) and Greg Galloway (USask), including analysis code by Nic Wayand. This study was supported by the Global Water Future programme funded by the Canada First Excellence Fund. Support from the Canadian Foundation for Innovation, Canada Research Chairs Program, and NSERC is gratefully acknowledged.

References

Barcons, J., Avila, M., & Folch, A. (2018). A wind field downscaling strategy based on domain segmentation and transfer functions: A wind field downscaling strategy based on domain segmentation and transfer functions. *Wind Energy*, *21*(6), 409–425. https://doi.org/10.1002/we.2169

Bernhardt, M., Schulz, K., Liston, G. E., & Zängl, G. (2012). The influence of lateral snow redistribution processes on snow melt and sublimation in alpine regions. *Journal of Hydrology*, *424–425*, 196–206. https://doi.org/10.1016/j.jhydrol.2012.01.001

Bernhardt, M., Zängl, G., Liston, G. E., Strasser, U., & Mauser, W. (2009). Using wind fields from a high-resolution atmospheric model for simulating snow dynamics in mountainous terrain. *Hydrological Processes*, *23*(7), 1064–1075. https://doi.org/10.1002/hyp.7208

Chang, K. (2008). *Introduction to geographic information systems*. McGraw-hill, McGraw-Hill.

DeBeer, C. M., & Pomeroy, J. W. (2009). Modelling snow melt and snowcover depletion in a small alpine cirque, Canadian Rocky Mountains. *Hydrological Processes*, *23*(18), 2584–2599. https://doi.org/10.1002/hyp.7346

Dornes, P., Pomeroy, J. W., Pietroniro, A., & Verseghy, D. L. (2008). Effects of spatial aggregation of initial conditions and forcing data on modeling snowmelt using a land surface scheme. *Journal of Hydrometeorology*, *9*(4), 789–803. https://doi.org/10.1175/2007jhm958.1

Dornes, P. F., Pomeroy, J. W., Pietroniro, A., Carey, S. K., & Quinton, W. L. (2008). Influence of landscape aggregation in modelling snow-cover ablation and snowmelt runoff in a sub-arctic mountainous environment. *Hydrological Sciences Journal*, *53*(4), 725–740. https://doi.org/10.1623/hysj.53.4.725

Essery, R., Li, L., & Pomeroy, J. (1999). A distributed model of blowing snow over complex terrain. *Hydrological Processes*, *13*(14–15), 2423–2438. https://doi.org/10.1002/(sici)1099-1085(199910)13:14/15<2423::aid-hyp853>3.0.co;2-u

Fang, X., & Pomeroy, J. W. (2009). Modelling blowing snow redistribution to prairie wetlands. In J. Buttle & B. Branfireun (Eds.), *Hydrological processes* (Vol. 23(18), pp. 2557–2569). https://doi.org/10.1002/hyp.7348

Fang, X., Pomeroy, J. W., DeBeer, C. M., Harder, P., & Siemens, E. (2019). Hydrometeorological data from Marmot Creek Research Basin, Canadian Rockies. *Earth System Science Data*, *11*(2), 455–471. https://doi.org/10.5194/essd-11-455-2019

Fang, X., Pomeroy, J. W., Ellis, C. R., MacDonald, M. K., DeBeer, C. M., & Brown, T. (2013). Multi-variable evaluation of hydrological model predictions for a headwater basin in the Canadian Rocky Mountains. *Hydrology and Earth System Sciences*, *17*(4), 1635–1659. https://doi.org/10.5194/hess-17-1635-2013

Farr, T. G., Rosen, P. A., Caro, E., Crippen, R., Duren, R., Hensley, S., et al. (2007). The shuttle radar topography mission. *Reviews of Geophysics*, *45*(2). https://doi.org/10.1029/2005rg000183

Fatichi, S., Vivoni, E. R., Ogden, F. L., Ivanov, V. Y., Mirus, B., Gochis, D., et al. (2016). An overview of current applications, challenges, and future trends in distributed process-based models in hydrology. *Journal of Hydrology*, *537*, 45–60. https://doi.org/10.1016/j.jhydrol.2016.03.026

Flügel, W. A. (1995). Modelling and management of sustainable basin-scale water resource systems. In *Proceedings of a Boulder Symposium*. IAHS Publcation No. 231.

Folch, A., Barcons, J., Kozono, T., & Costa, A. (2017). High-resolution modelling of atmospheric dispersion of dense gas using TWODEE-2.1: Application to the 1986 Lake Nyos limnic eruption. *Natural Hazards and Earth System Sciences*, *17*(6), 861–879. https://doi.org/10.5194/nhess-17-861-2017

Forthofer, J. M., Butler, B. W., & Wagenbrenner, N. S. (2014). A comparison of three approaches for simulating fine-scale surface winds in support of wildland fire management. Part I. Model formulation and comparison against measurements. *International Journal of Wildland Fire*, *23*(7), 969–981. https://doi.org/10.1071/wf12089

Freudiger, D., Kohn, I., Seibert, J., Stahl, K., & Weiler, M. (2017). Snow redistribution for the hydrological modeling of alpine catchments. *Wiley Interdisciplinary Reviews: Water*, *4*(5), e1232. https://doi.org/10.1002/wat2.1232

Harder, P., Schirmer, M., Pomeroy, J., & Helgason, W. (2016). Accuracy of snow depth estimation in mountain and prairie environments by an unmanned aerial vehicle. *The Cryosphere*, *10*(6), 2559–2571. https://doi.org/10.5194/tc-10-2559-2016

Jackson, P. S., & Hunt, J. C. R. (1975). Turbulent wind flow over a low hill. *Quarterly Journal of the Royal Meteorological Society*, *101*(430), 929–955. https://doi.org/10.1002/qj.49710143015

Langs, L. E., Petrone, R. M., & Pomeroy, J. W. (2021). Subalpine forest water use behaviour and evapotranspiration during two hydrologically contrasting growing seasons in the Canadian Rockies. *Hydrological Processes*, *35*(5). https://doi.org/10.1002/hyp.14158

Lehning, M., Löwe, H., Ryser, M., & Raderschall, N. (2008). Inhomogeneous precipitation distribution and snow transport in steep terrain. *Water Resources Research*, *44*(7). https://doi.org/10.1029/2007wr006545

Liston, G. E., & Elder, K. (2006). A meteorological distribution system for high-resolution terrestrial modeling (MicroMet). *Journal of Hydrometeorology*, *7*(2), 217–234. https://doi.org/10.1175/jhm486.1

Liston, G. E., Haehnel, R. B., Sturm, M., Hiemstra, C. A., Berezovskaya, S., & Tabler, R. D. (2007). Simulating complex snow distributions in windy environments using SnowTran-3D. *Journal of Glaciology*, *53*(181), 241–256. https://doi.org/10.3189/172756507782202865

Liston, G. E., Perham, C. J., Shideler, R. T., & Cheuvront, A. N. (2016). Modeling snowdrift habitat for polar bear dens. *Ecological Modelling*, *320*, 114–134. https://doi.org/10.1016/j.ecolmodel.2015.09.010

Luce, C. H., Tarboton, D. G., & Cooley, K. R. (1998). The influence of the spatial distribution of snow on basin-averaged snowmelt. *Hydrological Processes*, *12*(10–11), 1671–1683. https://doi.org/10.1002/(sici)1099-1085(199808/09)12:10/11<1671::aid-hyp688>3.0.co;2-n

Lumbrazo, C., Bennett, A., Currier, W. R., Nijssen, B., & Lundquist, J. (2022). Evaluating multiple canopy-snow unloading parameterizations in SUMMA with time-lapse photography characterized by citizen scientists. *Water Resources Research*, *58*(6). https://doi.org/10.1029/2021wr030852

Lundquist, J. D., Dickerson-Lange, S., Gutmann, E., Jonas, T., Lumbrazo, C., & Reynolds, D. (2021). Snow interception modeling: Isolated observations have led to many land surface models lacking appropriate temperature sensitivities. *Hydrological Processes*, *35*(7). https://doi.org/10.1002/hyp.14274

Luo, W., Taylor, M. C., & Parker, S. R. (2008). A comparison of spatial interpolation methods to estimate continuous wind speed surfaces using irregularly distributed data from England and Wales. *International Journal of Climatology*, *28*(7), 947–959. https://doi.org/10.1002/joc.1583

MacDonald, M. K., Pomeroy, J. W., & Pietroniro, A. (2009). Parameterizing redistribution and sublimation of blowing snow for hydrological models: Tests in a mountainous subarctic catchment. *Hydrological Processes*, *23*(18), 2570–2583. https://doi.org/10.1002/hyp.7356

MacDonald, M. K., Pomeroy, J. W., & Pietroniro, a. (2010). On the importance of sublimation to an alpine snow mass balance in the Canadian Rocky Mountains. *Hydrology and Earth System Sciences*, *14*(7), 1401–1415. https://doi.org/10.5194/hess-14-1401-2010

Marsh, C. B., Pomeroy, J. W., Spiteri, R. J., & Wheater, H. S. (2019). A finite volume blowing snow model for use with variable resolution meshes. *Water Resources Research*, *56*(2). https://doi.org/10.1029/2019wr025307

Marsh, C. B., Pomeroy, J. W., & Wheater, H. S. (2020). The Canadian hydrological model (CHM) v1.0: A multi-scale, multi-extent, variable-complexity hydrological model – Design and overview. *Geoscientific Model Development*, *13*(1), 225–247. https://doi.org/10.5194/gmd-13-225-2020

Marsh, C. B., Spiteri, R. J., Pomeroy, J. W., & Wheater, H. S. (2018). Multi-objective unstructured triangular mesh generation for use in hydrological and land surface models. *Computers & Geosciences*, *119*, 49–67. https://doi.org/10.1016/j.cageo.2018.06.009

Marsh, P., & Pomeroy, J. W. (1996). Meltwater fluxes at an arctic forest-tundra site. *Hydrological Processes*, *10*(10), 1383–1400. https://doi.org/10.1002/(sici)1099-1085(199610)10:10<1383::aid-hyp468>3.0.co;2-w

Marsh, P., & Pomeroy, J. W. (1999). Spatial and temporal variations in snowmelt runoff chemistry, Northwest Territories, Canada. *Water Resources Research*, *35*(5), 1559–1567. https://doi.org/10.1029/1998wr900109

Mason, P., & Sykes, R. (1979). Flow over an isolated hill of moderate slope. *Quarterly Journal of the Royal Meteorological Society*, *105*(444), 383–395. https://doi.org/10.1002/qj.49710544405

Milbrandt, J. A., Bélair, S., Faucher, M., Vallée, M., Carrera, M. L., & Glazer, A. (2016). The pan-Canadian high resolution (2.5 km) deterministic prediction system. *Weather and Forecasting*, *31*(6), 1791–1816. https://doi.org/10.1175/waf-d-16-0035.1

Mills, S. C., Brocq, A. M. L., Winter, K., Smith, M., Hillier, J., Ardakova, E., et al. (2019). Testing and application of a model for snow redistribution (Snow_Blow) in the Ellsworth mountains, Antarctica. *Journal of Glaciology*, *65*(254), 957–970. https://doi.org/10.1017/jog.2019.70

Mott, R., Schirmer, M., Bavay, M., Grünewald, T., & Lehning, M. (2010). Understanding snow-transport processes shaping the mountain snow-cover. *The Cryosphere*, *4*(4), 545–559. https://doi.org/10.5194/tc-4-545-2010

Mott, R., Vionnet, V., & Grünewald, T. (2018). The seasonal snow cover dynamics: Review on wind-driven coupling processes. *Frontiers of Earth Science*, *6*, 197. https://doi.org/10.3389/feart.2018.00197

Musselman, K. N., Pomeroy, J. W., Essery, R. L. H., & Leroux, N. (2015). Impact of windflow calculations on simulations of alpine snow accumulation, redistribution and ablation. *Hydrological Processes*, *29*(18), 3983–3999. https://doi.org/10.1002/hyp.10595

Nielsen, E. S. (2013). pyresample. Retrieved from https://pyresample.readthedocs.io/en/latest/

Pohl, S., Marsh, P., & Liston, G. E. (2006). Spatial-temporal variability in turbulent fluxes during spring snowmelt. *Arctic Antarctic and Alpine Research*, *38*(1), 136–146. https://doi.org/10.1657/1523-0430(2006)038[0136:svitfd]2.0.co;2

Pomeroy, J. W. (1991). Transport and sublimation of snow in wind-scoured alpine terrain. In *Snow, hydrology and forests in high alpine areas (proceedings of the IAHS vienna symposium)* (Vol. 205).

Pomeroy, J. W., Bernhardt, M., & Marks, D. (2015). Water resources: Research network to track alpine water. *Nature*, *521*(May), 32. https://doi.org/10.1038/521032c

Pomeroy, J. W., Brown, T., Fang, X., Shook, K., Pradhananga, D., Armstrong, R., et al. (2022). The cold regions hydrological modelling platform for hydrological diagnosis and prediction based on process understanding. *Journal of Hydrology*, *615*, 128711. https://doi.org/10.1016/j.jhydrol.2022.128711

Pomeroy, J. W., & Essery, R. L. H. (1999). Turbulent fluxes during blowing snow: Field tests of model sublimation predictions. *Hydrological Processes*, *13*(18), 2963–2975. https://doi.org/10.1002/(sici)1099-1085(19991230)13:18<2963::aid-hyp11>3.0.co;2-9

Pomeroy, J. W., Gray, D. M., Brown, T., Hedstrom, N. R., Quinton, W. L., Granger, R. J., & Carey, S. K. (2007). The cold regions hydrological model: A platform for basing process representation and model structure on physical evidence. *Hydrological Processes*, *21*(19), 2650–2667. https://doi.org/10.1002/hyp.6787

Pomeroy, J. W., & Li, L. (2000). Prairie and arctic areal snow cover mass balance using a blowing snow model. *Journal of Geophysical Research*, *105*(D21), 26619–26634. https://doi.org/10.1029/2000jd900149

Pomeroy, J. W., & Male, D. H. (1992). Steady-state suspension of snow. *Journal of Hydrology*, *136*(136), 275–301. https://doi.org/10.1016/0022-1694(92)90015-n

Pomeroy, J. W., Marsh, P., & Gray, D. M. (1997). Application of a distributed blowing snow model to the Arctic. *Hydrological Processes*, *11*(11), 1451–1464. https://doi.org/10.1002/(sici)1099-1085(199709)11:11<1451::aid-hyp449>3.0.co;2-q

Quill, R., Sharples, J. J., Wagenbrenner, N. S., Sidhu, L. A., & Forthofer, J. M. (2019). Modeling wind direction distributions using a diagnostic model in the context of probabilistic fire spread prediction. *Frontiers of Mechanical Engineering*, *5*, 5. https://doi.org/10.3389/fmech.2019.00005

Raleigh, M. S., Lundquist, J. D., & Clark, M. P. (2015). Exploring the impact of forcing error characteristics on physically based snow simulations within a global sensitivity analysis framework. *Hydrology and Earth System Sciences*, *19*(7), 3153–3179. https://doi.org/10.5194/hess-19-3153-2015

Ravazzani, G., Ceppi, A., & Davolio, S. (2020). Wind speed interpolation for evapotranspiration assessment in complex topography area. *Bulletin of Atmospheric Science and Technology*, *1*(1), 13–22. https://doi.org/10.1007/s42865-019-00001-5

Reynolds, D. S., Pflug, J. M., & Lundquist, J. D. (2021). Evaluating wind fields for use in basin-scale distributed snow models. *Water Resources Research*, *57*(2). https://doi.org/10.1029/2020wr028536

Ryan, B. C. (1977). A mathematical model for diagnosis and prediction of surface winds in mountainous terrain. *Journal of Applied Meteorology*, *16*(6), 571–584. https://doi.org/10.1175/1520-0450(1977)016<0571:ammfda>2.0.co;2

Schymanski, S. J., & Or, D. (2016). Wind increases leaf water use efficiency. *Plant, Cell and Environment*, *39*(7), 1448–1459. https://doi.org/10.1111/pce.12700

Serafin, S., Adler, B., Cuxart, J., De Wekker, S., Gohm, A., Grisogono, B., et al. (2018). Exchange processes in the atmospheric boundary layer over mountainous terrain. *Atmosphere*, *9*(3), 102. https://doi.org/10.3390/atmos9030102

Stewart, J. Q., Whiteman, C. D., Steenburgh, W. J., & Bian, X. (2002). A climatological study of thermally driven wind systems of the U.S. intermountain west. *Bulletin of the American Meteorological Society*, *83*(5), 699–708. https://doi.org/10.1175/1520-0477(2002)083<0699:acsotd>2.3.co;2

Sturm, M., McFadden, J. P., Liston, G. E., Chapin, F. S., Racine, C. H., & Holmgren, J. (2001). Snow-shrub interactions in Arctic Tundra: A hypothesis with climatic implications. *Journal of Climate*, *14*(3), 336–344. https://doi.org/10.1175/1520-0442(2001)014<0336:ssiiat>2.0.co;2

Sugita, M., Ogawa, S., & Kawade, M. (2020). Wind as a main driver of spatial variability of surface energy balance over a shallow 102-km^2 Scale Lake: Lake Kasumigaura, Japan. *Water Resources Research*, *56*(8). https://doi.org/10.1029/2020wr027173

Tabler, R. D., Pomeroy, J. W., & Santana, B. W. (1990). *Drifting snow* (pp. 95–145). American Society of Civil Engineers.

Vionnet, V., Fortin, V., Gaborit, E., Roy, G., Abrahamowicz, M., Gasset, N., & Pomeroy, J. W. (2020). Assessing the factors governing the ability to predict late-spring flooding in cold-region mountain basins. *Hydrology and Earth System Sciences*, *24*(4), 2141–2165. https://doi.org/10.5194/hess-24-2141-2020

Vionnet, V., Marsh, C. B., Menounos, B., Gascoin, S., Wayand, N. E., Shea, J., et al. (2021). Multi-scale snowdrift-permitting modelling of mountain snowpack. *The Cryosphere*, *15*(2), 743–769. https://doi.org/10.5194/tc-15-743-2021

Vionnet, V., Martin, E., Masson, V., Lac, C., Bouvet, F. N., & Guyomarc'h, G. (2017). High-resolution large eddy simulation of snow accumulation in alpine terrain. *Journal of Geophysical Research: Atmospheres*, *122*(20), 11005–11021. https://doi.org/10.1002/2017jd026947

Viviroli, D., Dürr, H. H., Messerli, B., Meybeck, M., & Weingartner, R. (2007). Mountains of the world, water towers for humanity: Typology, mapping, and global significance. *Water Resources Research*, *43*(7), 1–13. https://doi.org/10.1029/2006wr005653

Wagenbrenner, N. S., Forthofer, J. M., Lamb, B. K., Shannon, K. S., & Butler, B. W. (2016). Downscaling surface wind predictions from numerical weather prediction models in complex terrain with WindNinja. *Atmospheric Chemistry and Physics*, *16*(8), 5229–5241. https://doi.org/10.5194/acp-16-5229-2016

Wagenbrenner, N. S., Forthofer, J. M., Page, W. G., & Butler, B. W. (2019). Development and evaluation of a Reynolds-Averaged Navier–Stokes solver in WindNinja for operational wildland fire applications. *Atmosphere*, *10*(11), 672. https://doi.org/10.3390/atmos10110672

Walmsley, J. L., Taylor, P. A., & Keith, T. (1986). A simple model of neutrally stratified boundary-layer flow over complex terrain with surface roughness modulations (MS3DJH/3R). *Boundary-Layer Meteorology*, *36*(1–2), 157–186. https://doi.org/10.1007/bf00117466

Walmsley, J. L., Taylor, P. A., & Salmon, J. R. (1984). Simple guidelines for estimating wind speed variations due to small scale topographic features. *Climatological Bulletin*, *23*(1), 3–14.

Walmsley, J. L., Taylor, P. A., & Salmon, J. R. (1989). Simple guidelines for estimating wind speed variations due to small-scale topographic features - An update. *Climatological Bulletin*, *23*(1).

Wang, Z., & Huang, N. (2017). Numerical simulation of the falling snow deposition over complex terrain. *Journal of Geophysical Research: Atmospheres*, *122*(2), 980–1000. https://doi.org/10.1002/2016jd025316

Wayand, N. E., Marsh, C. B., Shea, J. M., & Pomeroy, J. W. (2018). Globally scalable alpine snow metrics. *Remote Sensing of Environment*, *213*, 61–72. https://doi.org/10.1016/j.rse.2018.05.012

Winstral, A., Elder, K., & Davis, R. E. (2002). Spatial snow modeling of wind-redistributed snow using terrain-based parameters. *Journal of Hydrometeorology*, *3*(5), 524–538. https://doi.org/10.1175/1525-7541(2002)003<0524:ssmowr>2.0.co;2

Winstral, A., Jonas, T., & Helbig, N. (2017). Statistical downscaling of gridded wind speed data using local topography. *Journal of Hydrometeorology*, *18*(2), 335–348. https://doi.org/10.1175/jhm-d-16-0054.1

Winstral, A., Marks, D., & Gurney, R. (2009). An efficient method for distributing wind speeds over heterogeneous terrain. *Hydrological Processes*, *23*(17), 2526–2535. https://doi.org/10.1002/hyp.7141

Winstral, A., Marks, D., & Gurney, R. (2013). Simulating wind-affected snow accumulations at catchment to basin scales. *Advances in Water Resources*, *55*, 64–79. https://doi.org/10.1016/j.advwatres.2012.08.011

Woo, M., & Thorne, R. (2006). Snowmelt contribution to discharge from a large mountainous catchment in subarctic Canada. *Hydrological Processes*, *20*(10), 2129–2139. https://doi.org/10.1002/hyp.6205

Wood, N. (1995). The onset of separation in neutral, turbulent flow over hills. *Boundary-Layer Meteorology*, *76*(1–2), 137–164. https://doi.org/10.1007/bf00710894

Wood, N. (2000). Wind flow over complex terrain: A historical perspective and the prospect for large-eddy modelling. *Boundary-Layer Meteorology*, *96*(1–2), 11–32. https://doi.org/10.1023/a:1002017732694